Integral Boundary Layer Heat Transfer Prediction on Turbine Blades

by

William James Steptoe

B.S. Mechanical Engineering, Carnegie Mellon University (1987)

SUBMITTED IN PARTIAL FULFILLMENT OF THE
REQUIREMENTS FOR THE DEGREE OF

Master of Science
in
Aeronautics and Astronautics
at the
Massachusetts Institute of Technology

25 September 1989

Signature of Author _____
Department of Aeronautics and Astronautics
25 September 1989

Certified by _____
Professor Alan H. Epstein
Thesis Supervisor

Certified by _____
Professor Marc Drela
Thesis Supervisor

Accepted by _____
Professor Harold Y. Wachman
Chairman, Departmental Graduate Committee

Contents

Abstract

Integral Boundary Layer Heat Transfer Prediction

on Turbine Blades

by

William James Steptoe

Submitted to the department of Aeronautics and Astronautics on September 25, 1989

in partial fulfillment of the requirements for the degree of

Master of Science in Aeronautics and Astronautics

An integral method for predicting heat transfer and losses in the boundary layer of a two dimensional airfoil is developed. Losses and heat transfer are measured by the momentum thickness and enthalpy thickness respectively. These integral parameters are calculated by the forward integration of three simultaneous differential equations using closure relations developed from the Falkner-Skan wedge flows. Local heat transfer measurements are obtained from a new empirical integral formula developed from finite difference solutions.

Comparison with finite difference solutions is good. Comparison with experiments is as good as finite difference prediction for the same flows. Further development should lead to integration into an integral boundary layer airfoil analysis and design tool and hence the ability to analyse and design non-adiabatic airfoils such as those in an axial flow turbine.

Thesis Supervisor: Dr. Alan Epstein

Title: Associate Professor of Aeronautics and Astronautics

ACKNOWLEDGEMENTS

The author would like to thank the following:

Professor Epstein for his supervision and motivation during this project.

Professor Drela for laying the groundwork for this thesis and helping me through the details.

Bob Haimes for his help with the computers.

My fellow students in the GTL who showed me the ropes.

All my friends from MIT, NPC, BUM, and CMU with whom I spent my liesure time.

And my family, especially my parents, Bill and Margaret Steptoe, who encourage me all the time.

This research was supported by the AFRAPT program grant AFOSR-85-0288 and the Air Force Aeropropulsion and Power Laboratory contract no. F33615-87-C-2729, Dr. Charles MacArthur, technical monitor.

Chapter 1

Nomenclature

1.1 Subscripts

$()_{AW}$: adiabatic wall quantity

$()_e$: edge quantity

$()_0$: stagnation quantity

$()_P$: pressure surface quantity

$()_{REF}$: reference quantity

$()_S$: suction surface quantity

$()_w$: wall quantity

$()_\infty$: freestream quantity

1.2 Definitions

A = area

$C_D = \frac{1}{\rho_e U_e^3} \int \tau \frac{\partial u}{\partial \eta} d\eta$

$C_f = \frac{\tau_w}{\frac{1}{2}\rho_e U_e^2}$

C_p = specific heat at constant pressure

D = Diameter, Diffusion Factor

F_{1-2} = View Factor from object 1 to object 2

$H = \frac{\delta^*}{\theta}$

$H^* = \frac{\theta^*}{\theta}$

$H^{**} = \frac{\delta^{**}}{\theta}$

$H_2 = \frac{\delta_2}{\theta}$

$H_k = \frac{\delta_k^*}{\theta_k}$

$H_w = \frac{T_w}{T_{0e}}$

k = coefficient of thermal conductivity

L = streamwise arclength

L_{MB} = Mean Beam Length

M_e = Edge Mach Number

p = partial pressure

P = perturbation coefficient

Pr = Prandtl Number

q = local heat transfer

$Q = \frac{q_w}{\rho_e U_e C_p T_{0e}}$

r = temperature recovery factor, $\sqrt{Pr}$ in laminar flows

R = Reaction

Re = Reynolds Number

St = Stanton Number, $\frac{q_w}{\rho_e U_e C_p (T_{AW} - T_w)}$

T = temperature

$T_{AW} = T_e + \frac{\sqrt{\mathrm{Pr}}}{2} \frac{U_e^2}{C_p}$

TET = turbine entrance temperature

u = local streamwise velocity

U_∞ = freestream velocity

v = radial velocity, normal velocity

V = axial fluid velocity

V_θ = circumferential blade velocity

α = absorption

β = Falkner-Skan wedge flow parameter

γ = ratio of specific heats

δ° = deviation angle, the angle between the trailing edge angle of the turbine blade, and the fluid departure angle in the blade reference frame

$\delta^* = \int(1 - \frac{\rho u}{\rho_e U_e})dy$

$\delta^{**} = \int \frac{u}{U_e}(1 - \frac{\rho}{\rho_e})dy$

$\delta_2 = \int \frac{\rho u}{\rho_e U_e}(1 - \frac{T_0}{T_{0e}})dy$

$\delta_k^* = \int(1 - \frac{u}{U_e})dy$

δ_T = thermal boundary layer thickness

δ_U = velocity boundary layer thickness

ΔW = work across turbine stage

ϵ = emmittance

ς = efficiency

η = normalized normal boundary layer coordinate $\frac{y}{\delta_U}$

$\theta = \int \frac{\rho u}{\rho_e U_e}(1 - \frac{u}{U_e})dy$

$\theta^* = \int \frac{\rho u}{\rho_e U_e}(1 - \frac{u^2}{U_e^2})dy$

$\theta_k = \int \frac{u}{U_e}(1 - \frac{u}{U_e})dy$

μ = viscosity

ρ = local density

σ = solidity ($\frac{circumferencial\ spacing}{axial\ chord}$) or Stefan-Boltzman constant

Φ = non-dimensional flow coefficient

Ψ = non-dimensional work coefficient

ω = pressure loss coefficient $\left(\frac{\Delta \textit{ total pressure across the blade}}{\textit{total} - \textit{static pressure upstream of blade}}\right)$

Chapter 2

Introduction

A turbine blade design involves a series of tradeoffs. Aerodynamic efficiency, heat transfer, performance and structural concerns affect the final design. In the turbine, like the rest of the engine, overall efficiency is the guiding design principle. Historically, the aerodynamic efficiency of the blades has been the first criteria [17]. Secondly, structural constraints are imposed to insure that the blade will stand up to the hostile gas turbine environment. High turbine entry temperature (TET), pressure, and rotational speed combine to make this a very hostile environment indeed. Yet this environment is getting more hostile due to increasing TET. By increasing TET specific thrust in a turbofan can be increased [14].

Since cooling is treated almost as an afterthought it is not well represented in the initial design process. Cooling is accomplished by channelling high pressure air from the compressor through ducts in the blades and endwalls of the turbine (Fig. 2.1). On the first stages of the turbine, some of the cooling air is vented through small holes or slots on to the surface of the blade providing an insulating film to further reduce heat transfer. Since this cooling air is not at the same temperature as the main flow, less energy can be removed from it in the turbine stage than had it passed through the combustor [14]. The film cooling also reduces the efficiency of the turbine by mixing with the boundary layer flow and increasing drag on the blades. These losses can be termed cooling losses.

It is difficult to predict the heat transfer in a turbine stage due to several factors including high freestream turbulence, pressure gradients, uncertainty in the blade temperature, and three dimensional effects. Prediction of the transition point, heat transfer in the transitional flow, separation bubbles, separated flow and unsteady effects all combine to make heat transfer prediction something of a black art. In fact, the limit on TET is set by the precision of blade-

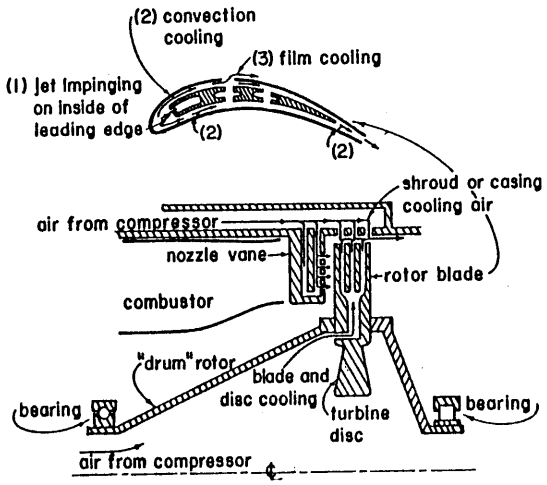

Figure 2.1: Schematic of air-cooled turbine, with cross section of cooled airfoil section at top [14, pg. 176]

cooling design techniques [14, pg. 197]. All modes of heat transfer must be considered when the total heat transfer, and therefore total heat to be removed is calculated.

Since the amount of cooling air needed for the design depends on the heat transfer predicted, uncertainty in the design is involved. Errors in the local heat transfer prediction and hence the surface temperature prediction can cause additional thermal stresses and shorten blade life. If the error is large, blade life could be short. In order to meet contractual obligations to blade life and efficiency several iterations of the build-test-teardown cycle are often necessary. Since each cycle can cost millions of dollars, it is useful to have a design tool that can accurately predict heat transfer and aerodynamic losses thereby reducing the number of necessary cycles.

What would happen if heat transfer were considered first, before the demands of aerodynamic efficiency? If the decrease in aerodynamic efficiency were low compared to the decrease in heat transfer, the tradeoff might raise the total cycle efficiency. The ISES airfoil design code written by Drela and Giles [6] uses integral boundary layer techniques and solves the inviscid

Euler equations for two-dimensional transonic cases. It can act as an analysis tool in which case it takes as input an airfoil shape and performs analysis at the desired conditions. It can also act as a design tool in which case it takes an airfoil and manipulates it toward achieving the specified criteria, be that drag, lift, or other parameter. With some modification ISES could be used to analyse heat transfer, and in the design mode manipulate an airfoil toward a specified heat transfer. From this, one could see how the tradeoff between aerodynamic efficiency and heat transfer would work, and reduce the number of build cycles required.

ISES has been shown to work well at designing and analyzing airfoils [6]. However, ISES boundary layer equations' boundary conditions specify that the wall be adiabatic. Since this is not the case on turbine airfoils this condition must be modified. By allowing heat transfer, lift and drag analysis can be done on non-adiabatic airfoils. In addition, to show the total heat transferred to the blade, a prediction of the local heat transfer based on the boundary layer must be made. Green [9] proposed a method of boundary layer and hence total heat transfer prediction based on forward integration of *three* simultaneous equations as opposed to the two used in ISES: the momentum-integral equation, the entrainment equation, and the total-energy equation [9, Eqns. 17, 19, and A-1]. In BLINT, the boundary layer module of ISES, the kinetic energy shape parameter equation is substituted for the entrainment equation as one of two equations. The other is the momentum-integral equation. When combined with the total-energy equation, we again have a three equation system. These equations are the basis of the aerodynamic performance and heat transfer prediction in this analysis code.

The computational time involved in solving the boundary layer and Euler equations depends very strongly on the number of variables. An integral non-adiabatic boundary layer code would have the advantage of having many fewer variables than a finite difference code. Hence, as ISES stands now an adiabatic integral boundary layer scheme is included, and the non-adiabatic modification developed in this thesis is also an integral method.

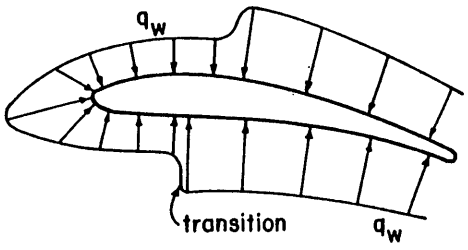

Figure 2.2: Distribution of heat transfer on a cooled turbine blade, showing sudden increase at boundary-layer transition to turbulent state [14, pg. 178]

Previous work by Nicholson [17] has shown that pressure surface heat transfer reduction can be achieved without significant reductions in aerodynamic efficiency. This reduction was achieved by tailoring the boundary layer not only near the laminar leading edge region, but also in the turbulent and relaminarized regions downstream. However, since the highest local levels of heat transfer are found near the leading edge of the blade in the laminar region (Fig. 2.2 [14]), the fraction of heat transferred in this region might be a high fraction of the total heat transfer depending on the length of the blade. Optimization of the leading edge laminar region, which this analysis code aides in, could lead to significant reductions on the total blade heat transfer. This code is the first step in modifying ISES to handle all non-adiabatic flows.

This analysis code takes as input an edge velocity distribution, the Reynolds number, Re_L, the Prandtl number, Pr, and the wall to freestream stagnation temperature ratio, H_w. Output is θ, δ^*, and δ_2, as well as the local integral parameters and heat transfer. From these both heat transfer and losses due to the boundary layer can be examined.

This thesis will describe and demonstrate a laminar integral heat transfer code that is the first step in developing a non-adiabatic ISES airfoil design code. The different modes of heat transfer will be examined to determine their relative contributions to the heat transfer problem. The trade off between designing for aerodynamic efficiency and designing for low heat transfer will be examined. Finally, the motivation behind developing an integral boundary layer heat transfer code, its development and testing against finite difference codes and experiment, and some recommendations for future work will be discussed.

Chapter 3

Modes of Heat Transfer

This chapter will examine the relative contributions of the three modes of heat transfer in a turbine environment. Radiation, conduction and convection will each be described and examined to see where the largest potential for heat transfer improvement lies.

3.1 Radiation

Radiation heat transfer is governed by the familiar Stefan-Boltzman law:

$$Q_{NET} = F_{1-2}\sigma A_1(T_1^4 - T_2^4) \tag{3.1}$$

where F is the view factor that depends on the geometry of the situation, A is the area, and σ is the Stefan-Boltzman constant. This formula is only valid for black bodies, that is bodies which emit according to the formula:

$$e(T) = \sigma T^4 \tag{3.2}$$

Since real objects are gray, that is they do not emit according to the above formula but some fraction thereof, the constant ϵ is added to the formula:

$$e(T) = \epsilon\sigma T^4 \tag{3.3}$$

where ϵ is the emittance. This is strictly valid only if ϵ is integrated over the entire electromagnetic spectrum, and in that case ϵ_T is called the total emittance. For a gas it is often difficult to find an equivalent ϵ_T since it depends on the pressure, the volume of the radiating gas, and the composition of the gas.

To find the radiative heat transfer between the products of combustion and a turbine blade the following approximation is used:

$$\frac{q}{A} = \epsilon_g(T_g)\sigma T_g^4 - \alpha_g(T_w)\sigma T_w^4 \tag{3.4}$$

[11] where $\alpha_g(T_w)$ is the absorptivity of the gas at the wall temperature (where $()_g$ designates a gas quantity). The geometry of the situation is taken into account through the emittance of the gas. Hottel and Sarafim [15] have devised a factor called the mean beam length, L_{MB}, which correlates the geometry and pressure into both the emittance and absorptivity of the gas. This method is not intended to be 100% accurate, but it does simplify the problem sufficiently to allow rapid evaluation. A complete discussion of gasious heat transfer can be found in Holman [11].

The combustion process will yield products that are different from air, and therefore these are the gasses that should be considered in the turbine blade radiation heat transfer problem. The combustor yields a mixture of oxygen, nitrogen, water vapor, and carbon dioxide, plus a few minor others depending on the fuel. The emittance of oxygen and nitrogen are small compared to the emittance of carbon dioxide and water vapor so they are neglected [11]. The emittance of carbon dioxide and water vapor depend on the pressure and temperature of the gasses, as well as the geometry of the turbine. Figure 3.1 shows the ratio of radiative to total heat transfer in a turbine. The convective heat transfer is calculated by assuming a representative Nusselt number from Guenette et al. [10] and several representative temperatures. At no point in the calculations does the ratio of radiative heat transfer to total heat transfer exceed 9%. With this in mind tackling the radiation heat transfer problem is not warranted since even a 10% reduction in radiative heat transfer results in less that a 1% total heat transfer reduction. See Appendix A for further explanation.

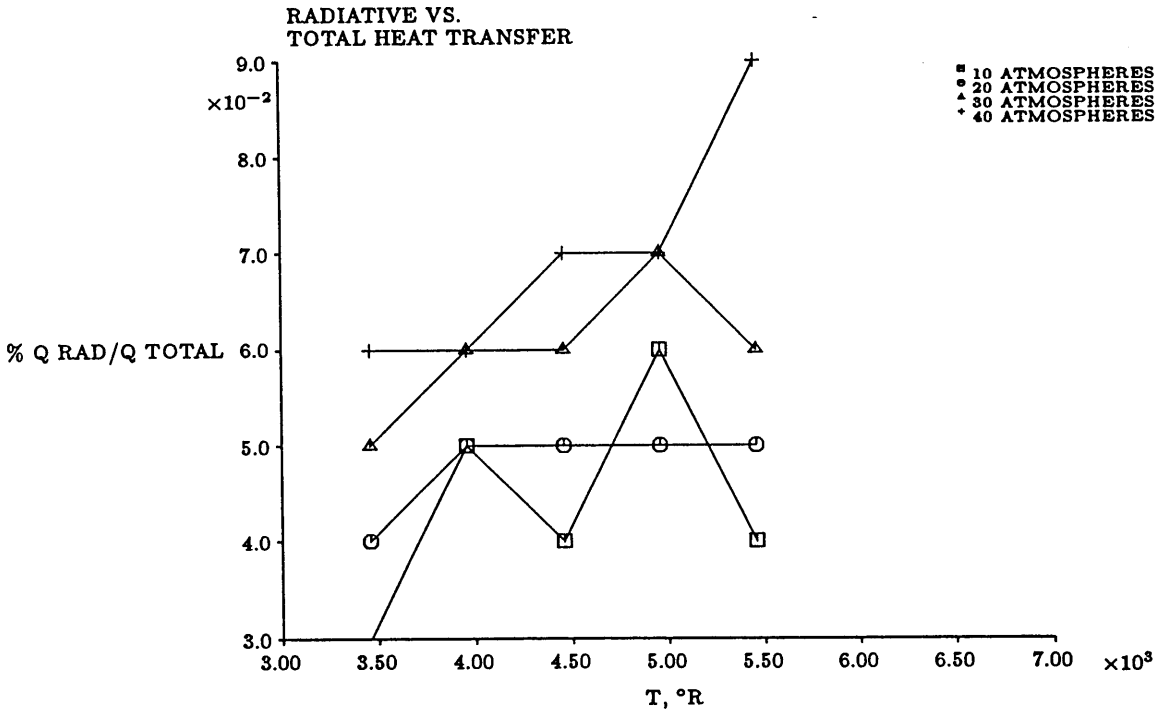

Figure 3.1: Radiative heat transfer/total heat transfer for four pressures as a function of temperature. Wall temperature was 2010° R. Gas was assumed to be products of combustion as described in Appendix A

3.2 Conduction

Turbine blades are currently made of metallic alloys. As such they have high coefficients of thermal conductivity, k. The result of this is that heat flows freely through the turbine blade, tending to equalize the temperature across the blade. However, the temperature is also driven by the local heat transfer which is decidedly non-uniform (Fig. 2.2). The various cooling schemes also tend to cool the blade unevenly, driving the blade to non-uniform temperatures. The net result is to have hot spots along the blade, especially at the leading edge where heat transfer is particularly high.

The interior arrangement of cooling ducts also influences the external temperature profile. Heat is conducted more easily through portions of the blade that are thick. Thin regions, such as the trailing edge, will be highly dependent on the external heat transfer to determine the blade temperature (Fig. 2.2). Thick regions also are more susceptible to thermal stress problems, so increasing the thickness to make the temperature distribution more uniform is not the answer.

3.3 Convection

Convection is the primary heat transfer mode in the turbine environment. Internally, heat is carried away from the surface by the circulating cooling air. Externally, heat is transferred to the blade due to the higher temperature combustion products. Convection is a function of the boundary layer temperature gradient as well as the heat transfer coefficient:

$$\frac{q}{A} = -k\frac{\partial T}{\partial y} \tag{3.5}$$

From Newton's law of cooling $\frac{q}{A} = h(T_w - T_{AW})_g$ so the heat transfer coefficient h is:

$$h = \frac{-k(\frac{\partial T}{\partial y})\mid_w}{(T_w - T_{AW})} \tag{3.6}$$

The driving temperature gradient for convective heat transfer in compressible boundary layers is $T_{AW} - T_w$. Non-dimensionalizing by the freestream stagnation temperature yields $\frac{T_{AW}}{T_{0e}} - \frac{T_w}{T_{0e}}$. $\frac{T_w}{T_{0e}}$ is named H_w. $\frac{T_{AW}}{T_{0e}}$ is defined as:

$$\frac{T_{AW}}{T_{0e}} = T_e + \frac{\frac{\sqrt{\Pr} U_e^2}{2C_p}}{T_e + \frac{U_e^2}{2C_p}}$$

or

$$\frac{T_{AW}}{T_{0e}} = \frac{2 + \sqrt{\Pr}(\gamma - 1)M_e^2}{2 + (\gamma - 1)M_e^2} \tag{3.7}$$

For $\Pr = 1$, $\frac{T_{AW}}{T_{0e}} = 1$. For $\Pr \neq 1$, $\frac{T_{AW}}{T_{0e}} \neq 1$, but if $\Pr \approx 1$ this ratio is essentially 1. Therefore the driving temperature gradient is approximately $1 - H_w$.

The heat transfer coefficient depends on several parameters but primarily on the thickness and nature of the boundary layer. Thin boundary layers conduct more heat than thick ones, turbulent boundary layers conduct more heat per unit thickness than do laminar boundary layers [11]. Convective heat transfer is most simply predicted by the Reynolds analogy (Eqn. 4.3). A new method of heat transfer prediction will be discussed in Section 5.3.

Each of the three modes of heat transfer has been examined. It was shown that although radiation plays a part in heat transfer it is a small one. The role of convection from the products of combustion plays the largest role in turbine heat transfer. Although much of a turbine blade's surface is probably turbulent, the laminar leading edge region is one of the highest regions of heat transfer due to the the very thin boundary layer. The model developed here will predict the local external convectional heat transfer for the laminar leading edge region (Fig. 2.2).

Chapter 4

Heat Transfer vs. Aerodynamic Efficiency

Gas turbine blade design has traditionally been concerned primarily with minimizing profile losses at a given blade loading. In order to examine the relationship between blade profile losses and heat transfer a method is needed that utilizes similar parameters to describe both the heat transfer and the blade profile losses. Although the diffusion factor method described in Ainley and Mathieson [1], Smith [21], Stewart, Whitney and Wong [22], NASA SP-36 [13], and Kerrebrock [14] is an approximate method, it allows the two factors to be compared without extensive computation. This simplification allows the problem to be generalized to any airfoil, and allows the two factors to be directly related. From this analysis heat transfer and profile loss trends can be examined, and the trade off between the two can be shown in a simple manner.

Several factors influence the blade drag: blade loading $\Psi = \frac{\Delta W}{V_\theta^2}$, is a measure of how much work can be extracted at a given turbine speed, $\Phi = \frac{V}{V_\theta}$ is the flow coefficient or non-dimensional mass flow. These two factors are related by the reaction, R, defined as the change in enthalpy across the rotor over the enthalpy change across the rotor and stator combined [12]. The diffusion factor, D, defined variously as

$$D = 1 - \frac{V_S}{V_P} \tag{4.1}$$

in [22] or

$$D = 1 - \frac{V_S}{V_P} + |\frac{v_2 - v_1}{2\sigma V_P}| \tag{4.2}$$

in [14] (where $v_2 - v_1$ is the change in tangential velocity) is an empirical correlation with the momentum thickness. ω measures the total pressure loss across the rotor and is a good measure of the 2-D rotor airfoil efficiency [14]. The deviation angle, $\delta°$, is the difference between the

trailing edge angle of the blade, and the exit angle of the gas. According to [14], $\delta^\circ \sim \frac{\Phi}{\sqrt{\sigma}}$; this is why as the solidity decreases, ω increases as the flow is not turned completely through the rotor.

The Reynolds analogy provides a first order method of comparing the local heat transfer with the diffusion factor through the blade solidity:

$$St = \frac{C_f}{2\,\mathrm{Pr}} \tag{4.3}$$

Q is a function of both St and σ, D is also a function of σ. Therefore the diffusion factor analysis of [14] can be used to compare the total pressure loss, ω, with the integrated total heat load, Q.

Figures 4.1 from [20] and 4.2 from [16] show two typical turbines at their operating points. The factor $\Phi\Psi$, the non-dimensional power output, is constant at all points on the figures. Any turbine operating at these conditions would have the same amount of power output per unit mass flow. These figures show lines of constant non-dimensional mass flow Φ. As the solidity decreases, the pressure loss coefficient increases until it is impossible to achieve the specified power output at any flow rate. Low solidity means a high deviation angle, hence low flow turning. It is easily seen that by deviating from the point of maximum aerodynamic efficiency to the left yields lower aerodynamic efficiency but also lower total heat transfer. An analysis of relative cycle costs, e.g. the price for a 1% aerodynamic efficiency increase, could show where the point of minimum total cycle costs would lie. From these graphs the trade off between aerodynamic efficiency and heat load can be seen clearly. Figures 4.1 and 4.2 show that the two turbines are operating at points slightly to the left of their predicted points of maximum aerodynamic efficiency, as would be predicted in light of the above discussion.

Although first order methods, the Reynolds analogy for predicting heat transfer, and the Diffusion Factor analysis for predicting aerodynamic efficiency have been combined to show the trade off between total heat transfer and aerodynamic efficiency. A point of maximum

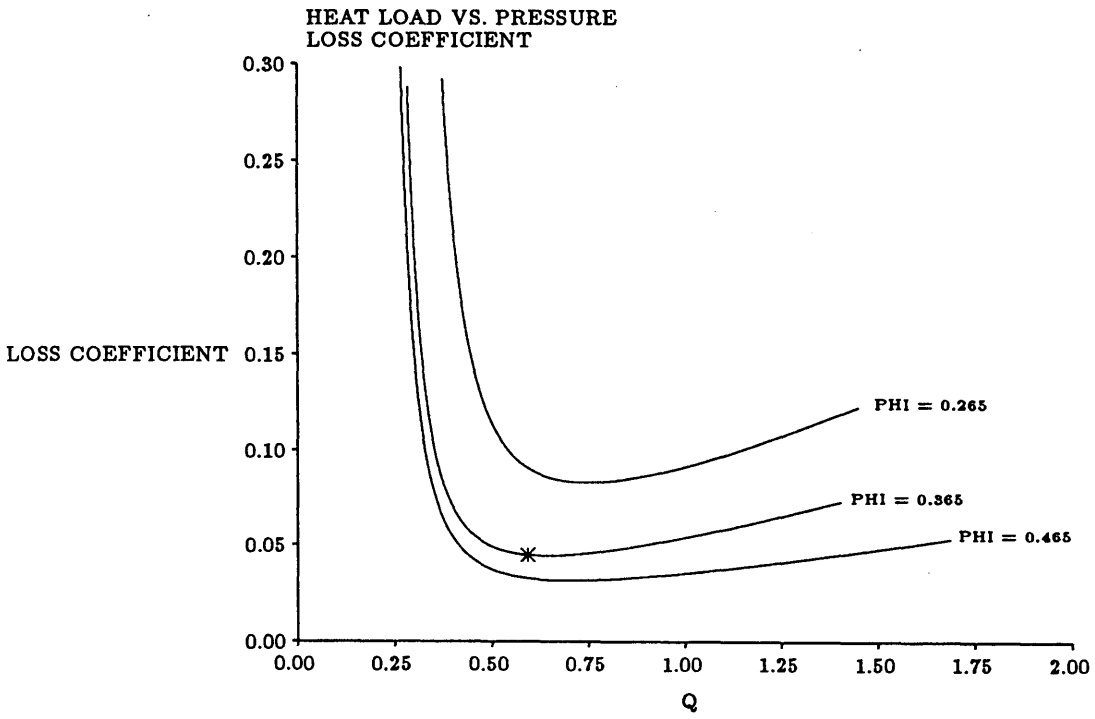

Figure 4.1: Pressure loss vs. heat load for a generic turbine with: reaction = 0.409, $\Phi\Psi$ = 0.405, solidity = 1.7, showing three mass flows. * designates the operating point of the NASA TM-83431 turbine which has these stated operating conditions.

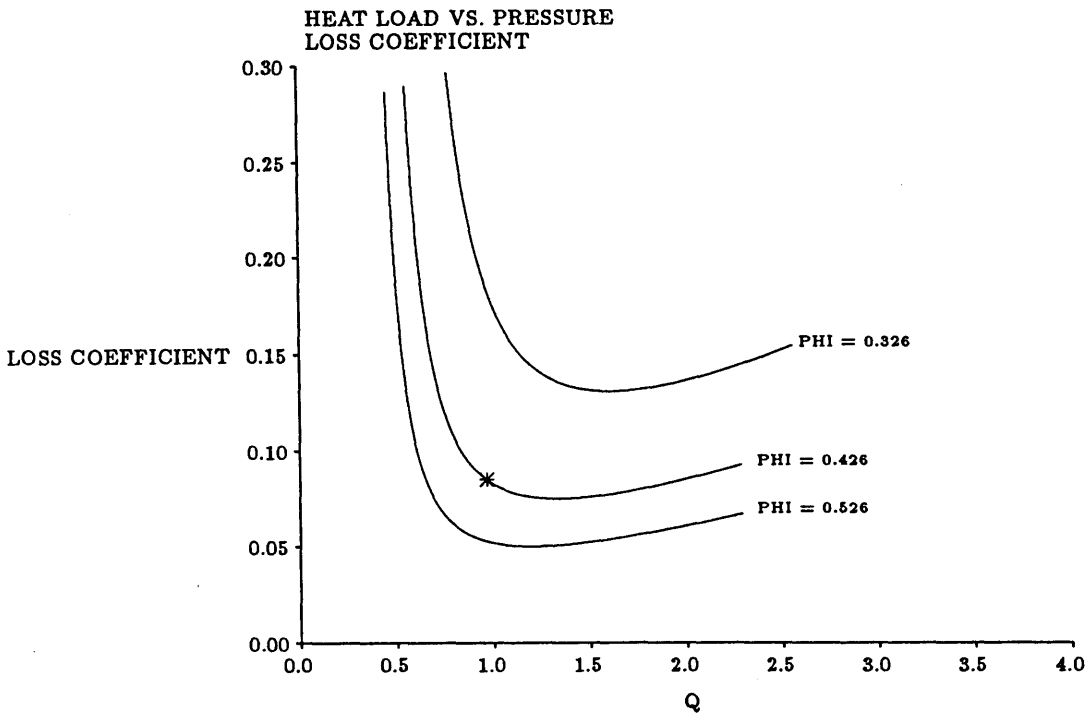

Figure 4.2: Pressure loss vs. heat load for a generic turbine with: reaction = 0.230, $\Phi\Psi = 0.666$, solidity = 1.7, showing three mass flows. * designates the operating point of the NRC/PWC turbine which has these stated operating conditions.

aerodynamic efficiency is shown to lie at some particular solidity for a given power output and mass flow rate. By deviating from this point lower total heat transfer may be attained at the cost of decreased aerodynamic efficiency. Depending on the relative costs of aerodynamic efficiency and cooling costs the point of minimum total losses (cooling plus aerodynamic) may or may not lie at the point of minimum aerodynamic losses. With the proper analysis tool, i.e. one that can predict both heat transfer and aerodynamic losses, this point of minimum total losses can be found more easily.

Chapter 5

Analysis Code

White [24] defines three types of computer generated boundary layer solutions: series expansion, finite difference, and approximate techniques. He goes on the further divide approximate techniques into integral methods, similarity patching, and weighted residual approaches. Series solutions are laborious, and are not suited for computational use. Finite difference solutions have the advantages that they are easily implemented on the computer, and are highly accurate, but have the disadvantage of being typically slower than integral methods. Integral methods have the advantages of being simple and computationally rapid. Drela and Giles [6] have written a design and analysis code (ISES) which uses the integral methods and has been shown to be highly accurate as well as rapid for two-dimensional adiabatic flows.

In order to handle turbine flows, which is the motivation for modifying ISES, the boundary layer solution scheme must be modified to handle non-adiabatic flows. Since BLINT is already structured to interface with ISES, it makes sense to use the format of BLINT with some modification to solve the non-adiabatic boundary layer equations. BLINT has the advantages over finite difference codes of being more computationally rapid. In addition, few integral heat transfer codes have been written.

5.1 Integral Boundary Layer Equations

The equations used in UNI are derived in Appendix B. By integrating across the boundary layer the resulting boundary layer equations are functions of only the streamwise coordinate and the integral boundary layer parameters (θ, δ^*, H etc.). For compressible flow the following

Kármán integral equations and the enthalpy equation result:

$$\frac{\partial \theta}{\partial x} + \frac{\theta}{U_e}\frac{dU_e}{dx}(2 + H - M_e^2) = \frac{C_f}{2} \tag{5.1}$$

$$\theta\frac{dH^*}{dx} + (2H^{**} - H^*(H-1))\frac{\theta}{U_e}\frac{dU_e}{dx} = 2C_D - H^*\frac{C_f}{2} \tag{5.2}$$

$$Q - H_2(\frac{C_f}{2} - (H+1)\frac{\theta}{U_e}\frac{dU_e}{dx}) = \theta\frac{dH_2}{dx} \tag{5.3}$$

These three simultaneous differential equations are integrated by marching downstream. The solution is the three dependent variables θ, δ^*, and δ_2. A Newton-Raphson solver is used to iteratively solve for the three variable at each streamwise position. The residual for each equation is found and driven toward zero. Each equation is linearized in essentially the same way as Chapter 6.10 of [5] except that the edge Mach number and velocities are treated as constants, since in UNI they are specified.

5.2 Dimensions and Non-dimensionalization

In the equations in this program most variables are naturally non-dimensionalized, that is they appear in forms like $\frac{u}{U_e}$, $\frac{\rho}{\rho_e}$ etc. (see Section 1.2). However, the input velocity vs. streamwise arclength must be non-dimensionalized. Choosing the simplest values possible, x is non-dimensionalized by L, the streamwise trailing edge arclength, and U_e is non-dimensionalized by the freestream speed of sound $a_0 = \sqrt{\gamma RT}$.

The dimensions on θ, δ^*, and δ_H are relatively easy to interpret. Each has a significant meaning: δ^* is the displacement thickness, that it is the distance that the inviscid flow is displaced from the edge of the airfoil. The momentum thickness also has an important meaning. It is the thickness of a stream of fluid with the edge velocity U_e, and edge density ρ_e that contains an amount of momentum equal to the momentum deficit in the boundary layer. The enthalpy thickness is similar to the momentum thickness. It is the thickness of a stream of fluid with the edge velocity U_e, edge density ρ_e, and edge stagnation temperature T_{0e} that contains an

amount of enthalpy equal to the enthalpy deficit in the boundary layer. This is significant in that this is the amount of enthalpy absorbed by the blade.

The other thicknesses, θ^*, and δ^{**}, the kinetic energy thickness and the density thickness are similarly the fluid stream thicknesses containing the same kinetic energy and mass as the kinetic energy and mass deficits in the boundary layer.

5.3 Unified Heat Transfer and Loss Prediction Code (UNI)

The code takes as input the edge flow velocity vs. streamwise distance, the Reynolds number Re_L, and the wall to freestream stagnation temperature ratio, H_w. To identify the particular gas involved and the dimensioned temperature of the flow the Prandtl number, Pr, at the flow conditions, a temperature correlation constant based on Pr, and the ratio of specific heats (γ) are also needed.

In order to close equations 5.1 through 5.3 five functional relations are needed in terms of the dependent variables and parameters:

$$H^* = H^*(H_k, M_e, Re_\theta) \tag{5.4}$$

$$H^{**} = H^{**}(H_k, M_e) \tag{5.5}$$

$$C_f = C_f(H_k, M_e, Re_\theta) \tag{5.6}$$

$$C_D = C_D(H_k, M_e, Re_\theta) \tag{5.7}$$

$$Q = Q(H_k, M_e, Re_\theta, H_w, H_2) \tag{5.8}$$

M_e^2 is obtained from the edge flow velocity at each streamwise coordinate [4]; Re_θ is a function of the solution variable θ. H_k, the kinematic shape parameter, relates the given flow to an equivalent incompressible flow through M_e^2, H_2 and H_w. Equations 5.4 through 5.7 are given in BLINT [5]. Two of the five, H^* and H^{**}, have no temperature dependence independent of H_k, therefore they can be used without modification from BLINT. C_D and C_f are dependent

on the local values of the viscosity, which is dependent on the local temperature and cannot be modelled effectively by H_k alone. C_f is corrected using the temperature-viscosity relation of Rayleigh [24].

$$\frac{\mu}{\mu_{REF}} = (\frac{T}{T_{REF}})^n \tag{5.9}$$

for air n=0.666 [24].

Since C_D depends on the integrated values of the viscosity the Rayleigh equation is not the proper correction. A correction to C_D based on Drela's finite difference code BLAKE [4] is included in UNI. The quantity $\tau \frac{\partial u}{\partial \eta}$ was integrated over the boundary layer at three H_w. This quantity and hence C_D was found to vary approximately as $0.2(1 - H_w)^2$ over the range of H_w tested ($0.6 \leq H_w \leq 1.0$).

Q, the local heat transfer, is predicted using an integral shape parameter relationship. This relationship was not needed for the adiabatic conditions of BLINT and was obtained empirically by observing solutions from BLAKE. The quantities H_k*C_f*(1-H_w) and St*H_2 were found for all the test cases and all the test profiles describes in Chapter 6. The resulting linear relationship for all points is shown in Figure 5.1. This relationship varies little with Re_L or freestream pressure gradient. It is definitely a function of Pr. As H_w approaches 1 (adiabatic conditions) the relationship is less accurate since the factor (1-H_w) approaches 0. This method of heat transfer prediction yields better results than the Reynolds analogy since that relationship was developed for flat plate flow and $Pr = 1$. Even when corrected for pressure gradient (Fig. 5.2 [24, pg. 286]) the new relationship gives better agreement with the finite difference code results. Reynolds analogy corrected for pressure gradient is:

$$St_x = \frac{C_{fx}}{2Pr^{\frac{2}{3}} \frac{f_0''}{G(1,\beta)}} \tag{5.10}$$

This new relationship is interesting in its simplicity. Deviation from the linear results is greatest at the points of high acceleration (Fig. 5.1, near the origin). No Re_L dependence at all was

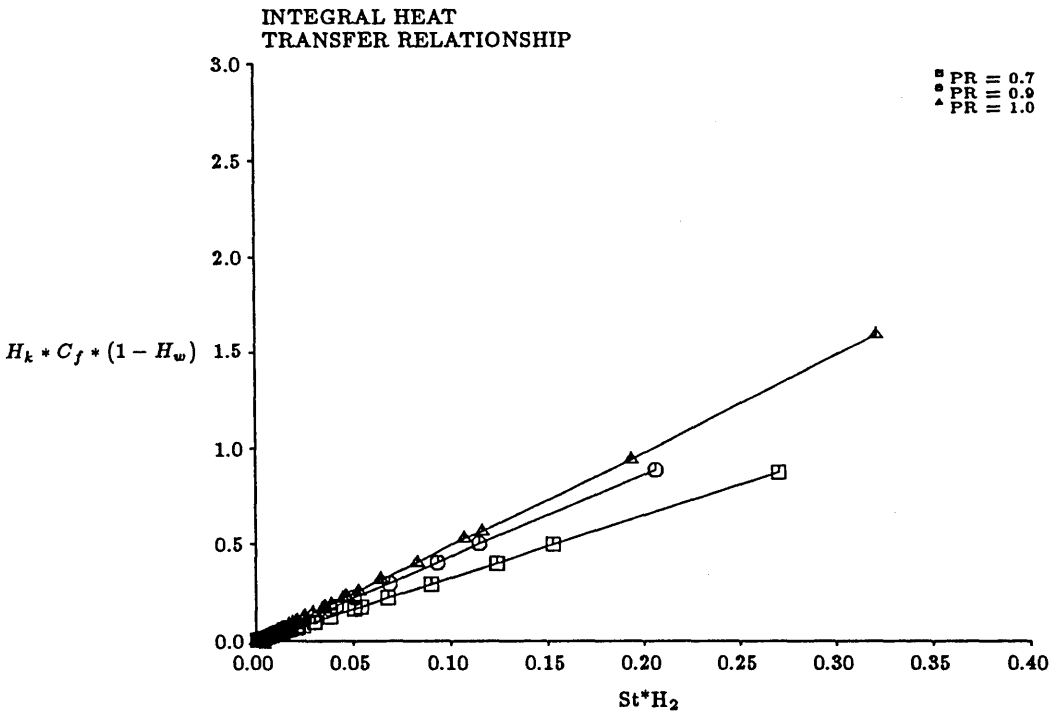

Figure 5.1: Integral correlation to determine the local heat transfer coefficient, derived from BLAKE results. Y-axis is a measure of surface friction and the driving temperature gradient, X-axis is a measure of heat transfer coefficient

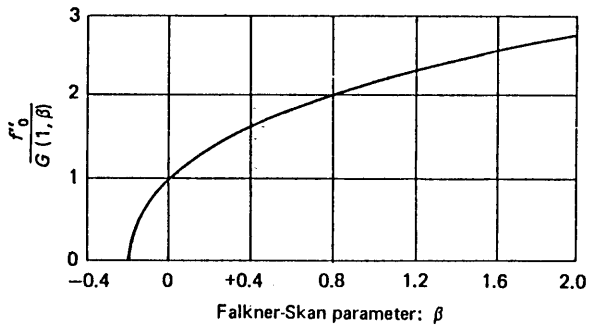

Figure 5.2: Reynolds analogy variation with β, the Falkner-Skan freestream pressure gradient coefficient [24, pg. 286]

observed. It is also surprising in its accuracy since it predicts the actual heat transfer as well as heat transfer trends quite well.

H_k relates the actual flow to an equivalent incompressible flow. In BLINT the only source of compressibility is through Mach number effects. However, since there is now a temperature gradient this effect must also be accounted for. In BLINT the relationship between H_k and H is a simple algebraic one through M_e^2 [5].

$$H_k = \frac{H - 0.290M_e^2}{1 + 0.113M_e^2} \tag{5.11}$$

To account for the effects of temperature a more complicated relationship has been developed.

Since M_e^2 is known from the external flow, and H_w is given, H and H_2 are functions of the one free parameter, H_k. H and H_2 depend on the velocity and temperature boundary layer profiles, so in order to correlate H_k to H and H_2, it is necessary to define the boundary layer profiles in terms of H_k. The boundary layer velocity profile has the following boundary

conditions:

$$\begin{aligned} u(1) &= 1 \\ u(0) &= 0 \\ u^N(1) &= 0 \end{aligned}$$

where N = I to ∞ (derivatives with respect to η).

In the tradition of Pohlhausen (1921) [24] an approximate velocity profile was chosen as a polynomial of η. Several velocity profiles using only integer exponents of η were attempted. It was found that with these formulae it is impossible to attain $H_k = 2$. In fact, by approximating u(η) with N terms (u(η) = $A_1\eta + A_2\eta^2 + \cdots + A_N\eta^N$) the limit as N$\rightarrow\infty$ reaches $H_k = 2$. By using a fractional exponent (in this case $\sqrt{\eta}$) it is possible to reach much lower H_k, (in this case $H_k \approx 1.6$). $H_k = 2$ is the lowest H_k that is physically possible without a velocity overshoot [24]. A third order polynomial was used in order to capture the three boundary conditions

$$\begin{aligned} u(1) &= 1 \\ u(0) &= 0 \\ u'(1) &= 0 \end{aligned}$$

and an integral condition such that when u(η) is substituted into the definition of H_k, the specified H_k results. A higher order polynomial could have been used but this would have seriously complicated the tedious task of defining the polynomial coefficients in terms of H_k. Since the three boundary conditions are fixed, the shape of the boundary layer velocity profile is dependent only on H_k.

A temperature profile is assumed across the boundary layer as well $\frac{T_0}{T_{0e}} = \frac{T_0}{T_{0e}}(\eta)$. The boundary conditions on this are:

$$\frac{T_0}{T_{0e}}(0) = H_w \qquad (5.12)$$

$$\frac{T_0}{T_{0e}}(1) = 1 \tag{5.13}$$

The baseline temperature profile shape is that for a flat plate at the given H_w [24]. This shape is varied by a perturbation function $P\eta(1-\eta)$ where P is the perturbation coefficient.

Since the stagnation temperature ratio is specified yet the density gradient depends on the static temperature ratio, the static temperature ratio is a derived quantity. This requires that the temperature and velocity gradients in the boundary layer be coupled. We know that for flows where $Pr \neq 1$ the thicknesses δ_T and δ_U are not identical. For laminar flow an empirical relationship has been developed to relate δ_T and δ_U:

$$\frac{\delta_T}{\delta_U} = Pr^{0.42} \tag{5.14}$$

[24]

The solution process is iterative using a Newton-Raphson solver starting at an estimated H and H_2, guessing H_k and P, substituting the resulting velocity and temperature distributions into the definitions of H_k and H_2, then correcting H_k based on the resulting H, and correcting P based on the resulting value of H_2. The resulting H_k is used to define the quantities in Equations 5.4 through 5.8. These are substituted into the residuals of Eqs. 5.1 through 5.3. If the residuals are larger than the prescribed maxima, a correction is calculated for δ^*, θ, and δ_2, and the process repeats.

The result is an integral, non-adiabatic boundary layer solution scheme similar in form to Drela's BLINT code. This scheme can be implemented to determine the heat transfer and profile losses for a non-adiabatic laminar airfoil. It is the first step in modifying the ISES airfoil design and analysis code to handle turbine airfoils.

Chapter 6

Test Cases

6.1 Development

During the development process the unified heat transfer and loss prediction code was checked against Drela's finite difference code BLAKE [4]. Several freestream velocity profiles were developed as test profiles; these were implemented at different M_e, Pr, H_w, and Re_L, where Re_L is in terms of the streamwise arclength. The development test profiles were: flat plate (constant velocity), a Falkner-Skan wedge flow with $\beta = 0.5$ (parabolic velocity profile), and a simulated airfoil profile with flow from a stagnation point over a circular cylinder to the maximum velocity ($2U_\infty$) followed by a flat plate region, then decreasing velocity until separation (sinusoidal velocity increase followed by constant velocity, then a velocity decrease) (Figs. 6.1, 6.2, and 6.3). U_e is given in terms of the leading edge speed of sound.

Since the code is intended to be used for turbine blade analysis the test conditions were designed to simulate typical turbine leading edge flows. The development test parameter space was:

$$
\begin{aligned}
0.0 < \quad & M_e \quad < 1.0 \\
0.7 < \quad & Pr \quad < 1.0 \\
1.0 \times 10^5 < \quad & Re_L \quad < 1.0 \times 10^7 \\
0.6 < \quad & H_w \quad < 1.0
\end{aligned}
$$

Tests were conducted by prescribing Pr, H_w, and Re_L for the flow, and allowing M_e to be calculated from the specified velocity. Identical conditions were specified for both UNI and BLAKE, so the solutions were directly comparable. (Table 6.1).

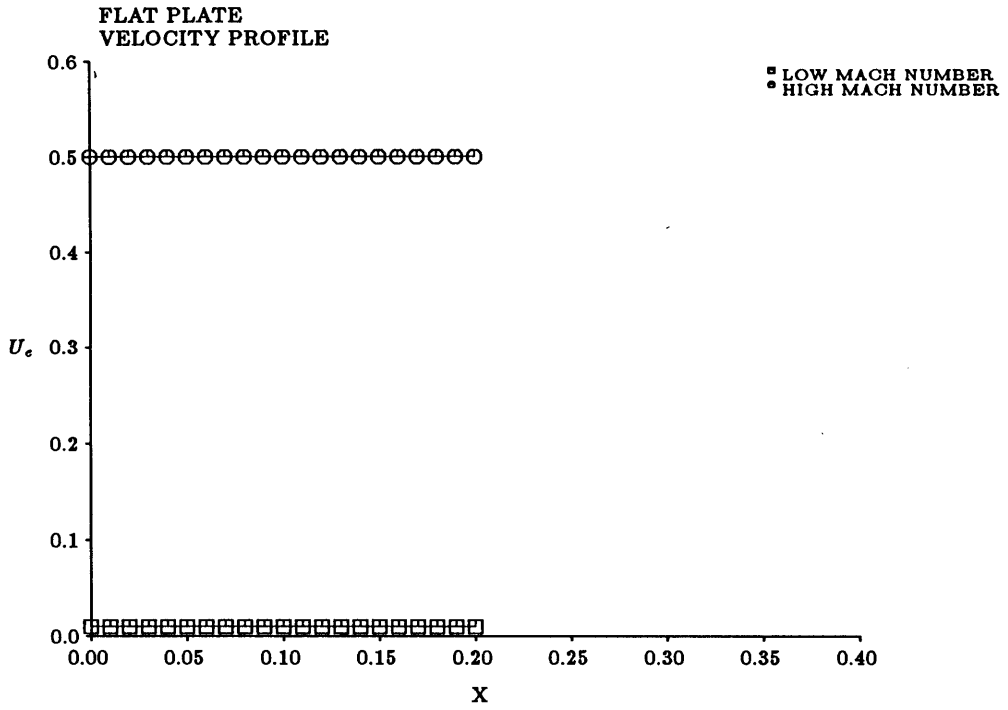

Figure 6.1: Flat plate profiles

1. $Pr = 0.7$, $Re = 1.0 \times 10^5$
2. $Pr = 1.0$, $Re = 1.0 \times 10^5$
3. $Pr = 0.7$, $Re = 5.0 \times 10^6$
4. $Pr = 1.0$, $Re = 5.0 \times 10^6$
5. $Pr = 0.7$, $Re = 1.0 \times 10^7$
6. $Pr = 1.0$, $Re = 1.0 \times 10^7$

Table 6.1: List of developmental test cases

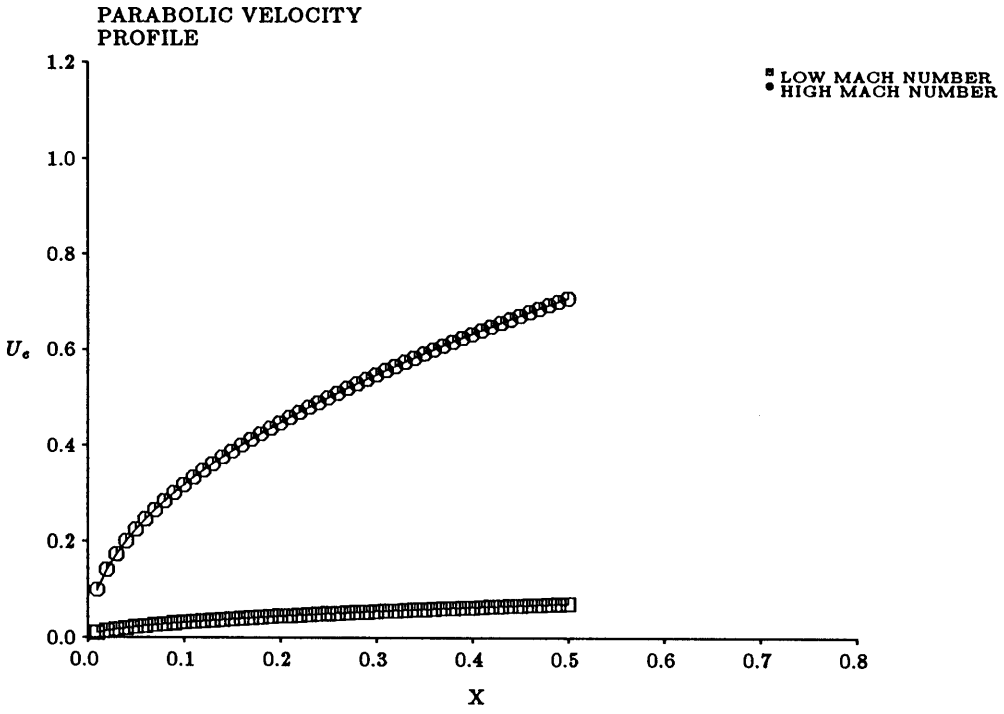

Figure 6.2: Parabolic profiles

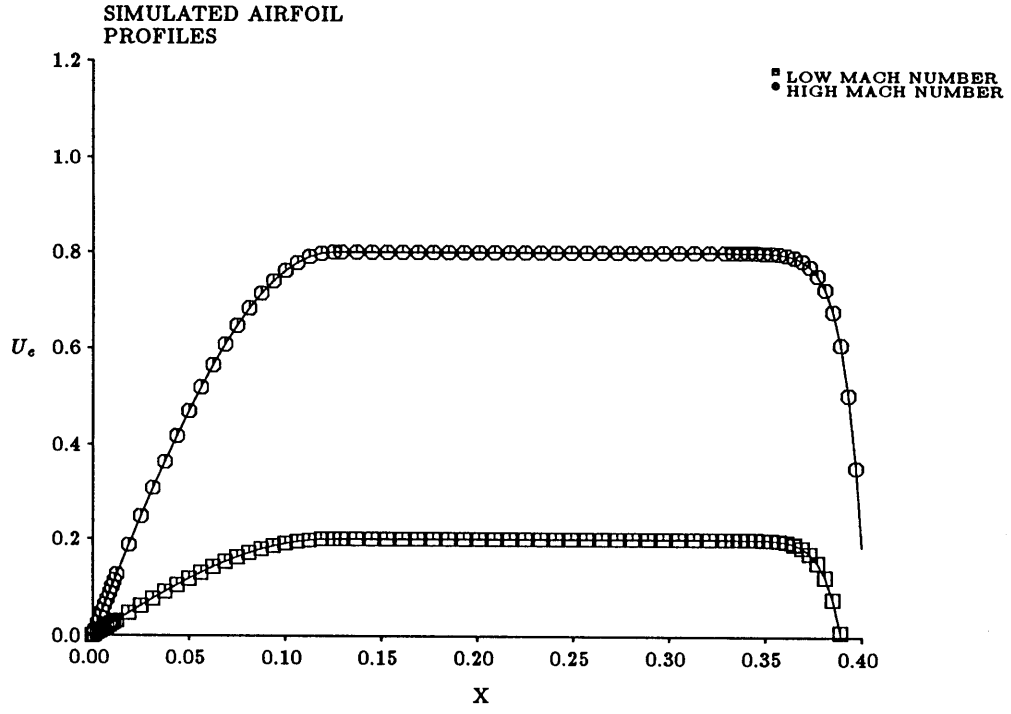

Figure 6.3: Simulated airfoil profiles

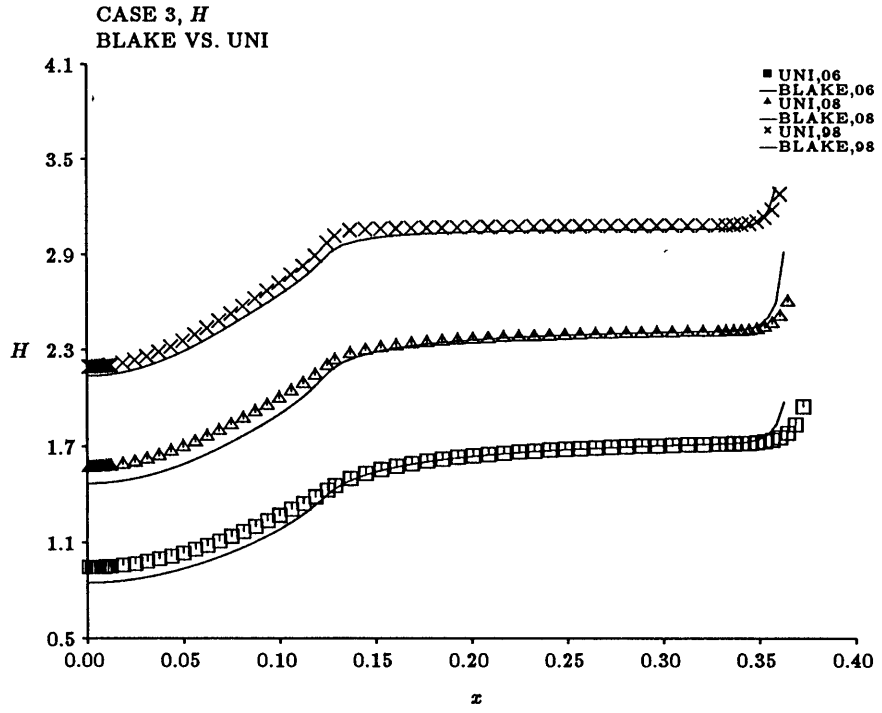

Figure 6.4: Case 3, H vs. x. For all cases 3 and 4, the individual points are UNI results, the solid lines indicate the BLAKE solution at the same H_w

Implementing UNI and BLAKE yields several output variables. Since the loss and heat transfer measurements are of greatest interest, these were the results that were directly compared. Loss calculations were compared through the shape parameter H, heat transfer calculations through the enthalpy thickness shape parameter H_2. In addition, local values of C_f and Stanton number were compared. Since the integral parameters scale with the Reynolds number, the shape factors H and H_2 are identical for the range of Reynolds numbers tested.

Figures 6.4 through 6.16 show a comparison between finite difference results from BLAKE and integral results from UNI. The plots are for $Re = 5.0\times10^6$. In case 3, $Pr = 0.7$, and case 4, $Pr = 1.0$. Both are for the high Mach number simulated airfoil flow (see Figure 6.3). The simulated airfoil case was chosen to represent the developmental cases because of its full sweep of shape parameter values, from stagnation point to separation.

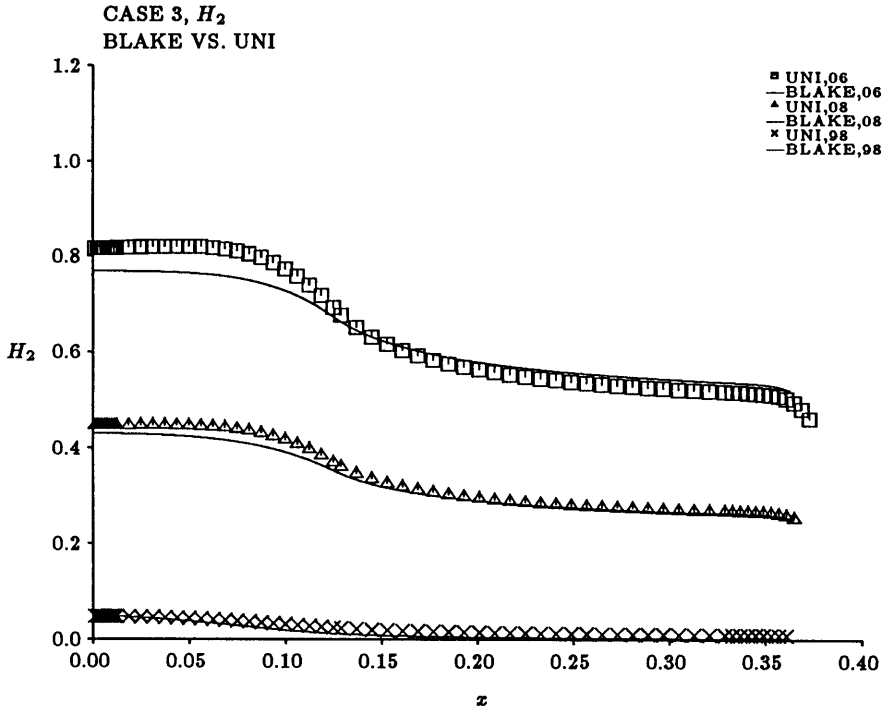

Figure 6.5: Case 3, H_2 vs. x

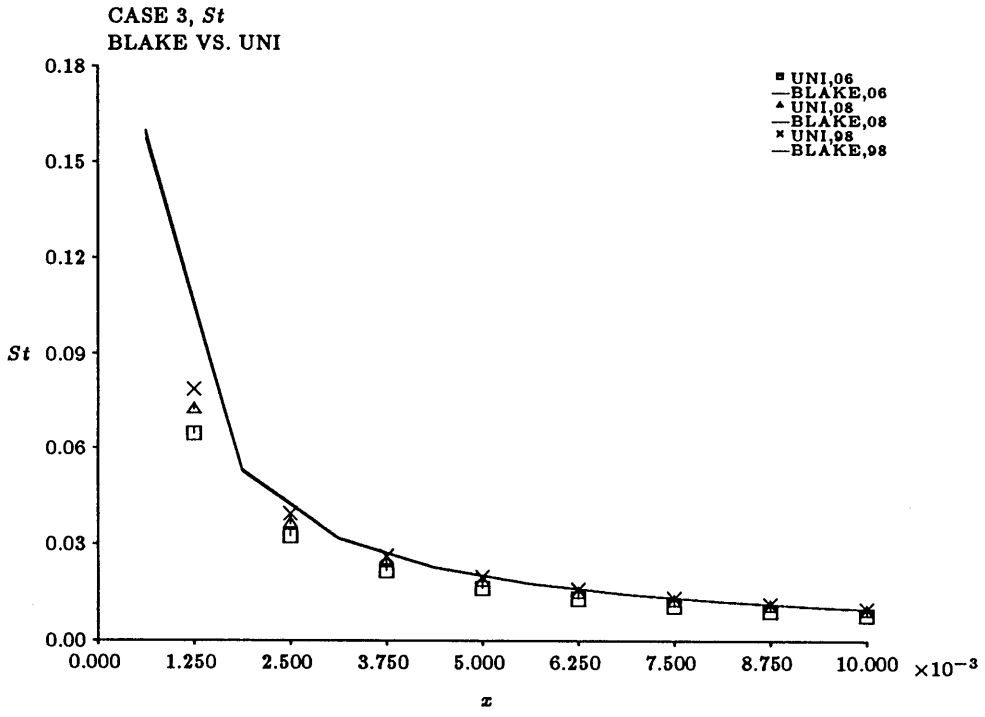

Figure 6.6: Case 3, Stanton Number vs. x, Leading Edge

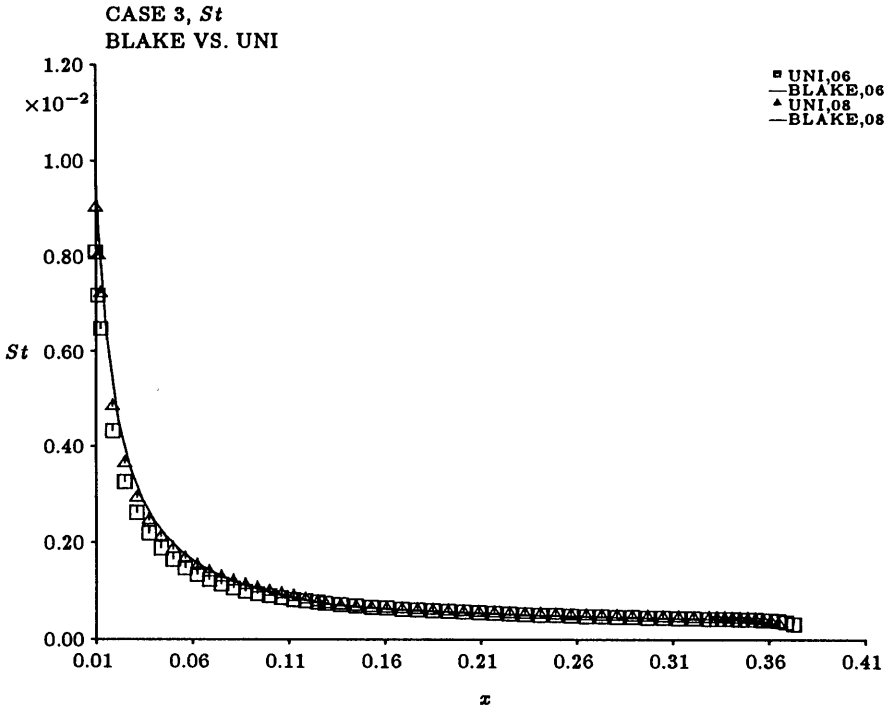

Figure 6.7: Case 3, Stanton Number vs. x, Downstream of leading edge

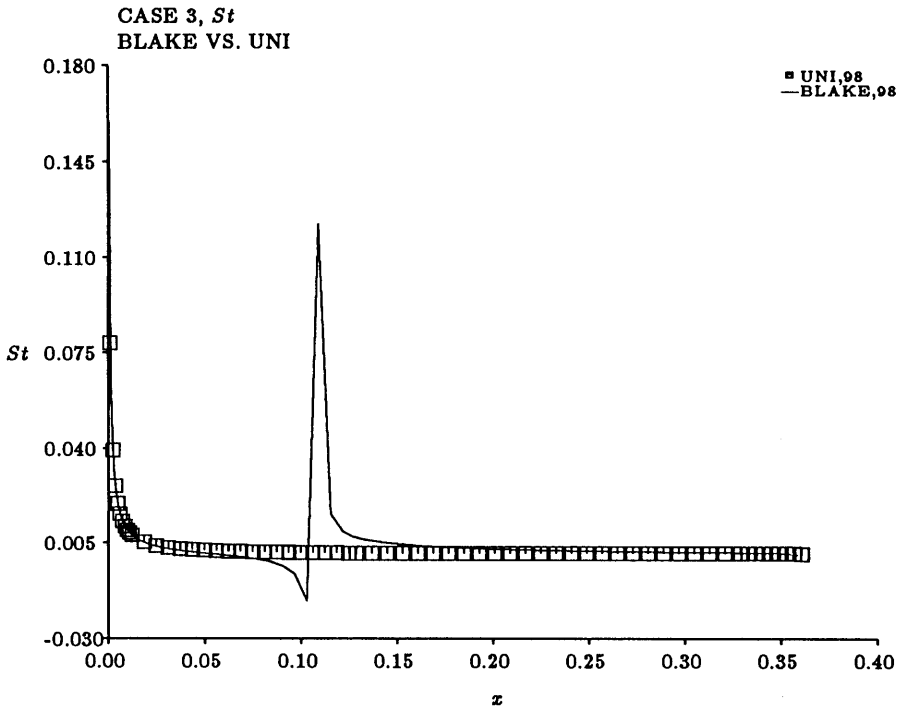

Figure 6.8: Case 3, Stanton Number vs. x, $H_w = 0.98$. At the point in the flow where $\frac{T_{AW}}{T_{0e}} - H_w = 0.0$, (for this case $M_e = 0.8325$) the denominator of the Stanton number goes to zero. Since the driving temperature gradient goes from positive to negative, the heat transfer, Q, changes sign at this point.

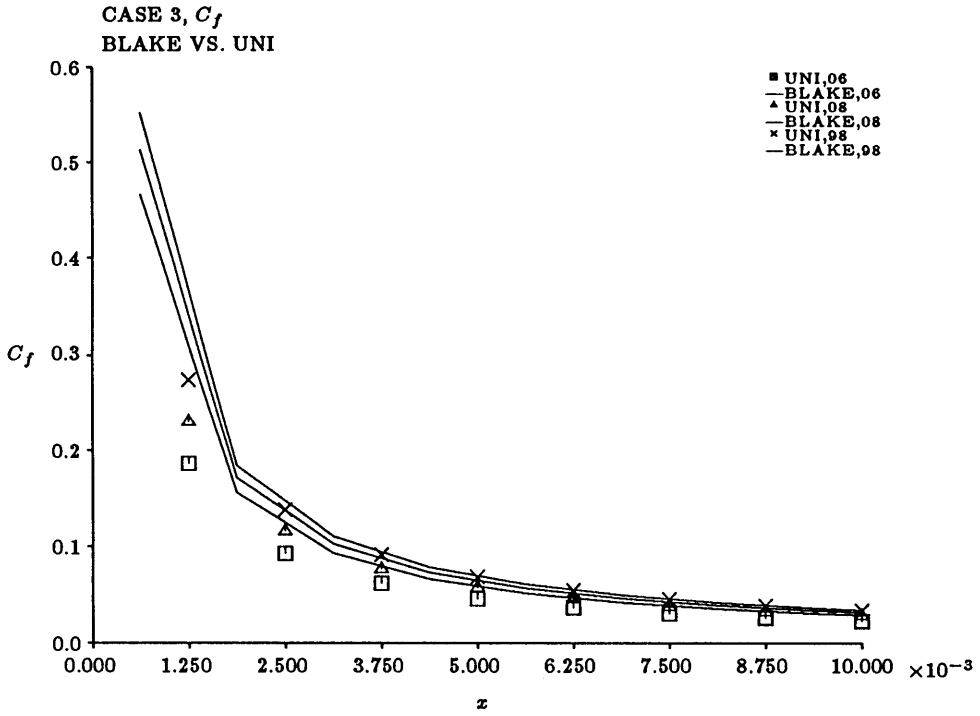

Figure 6.9: Case 3, C_f vs. x, Leading Edge

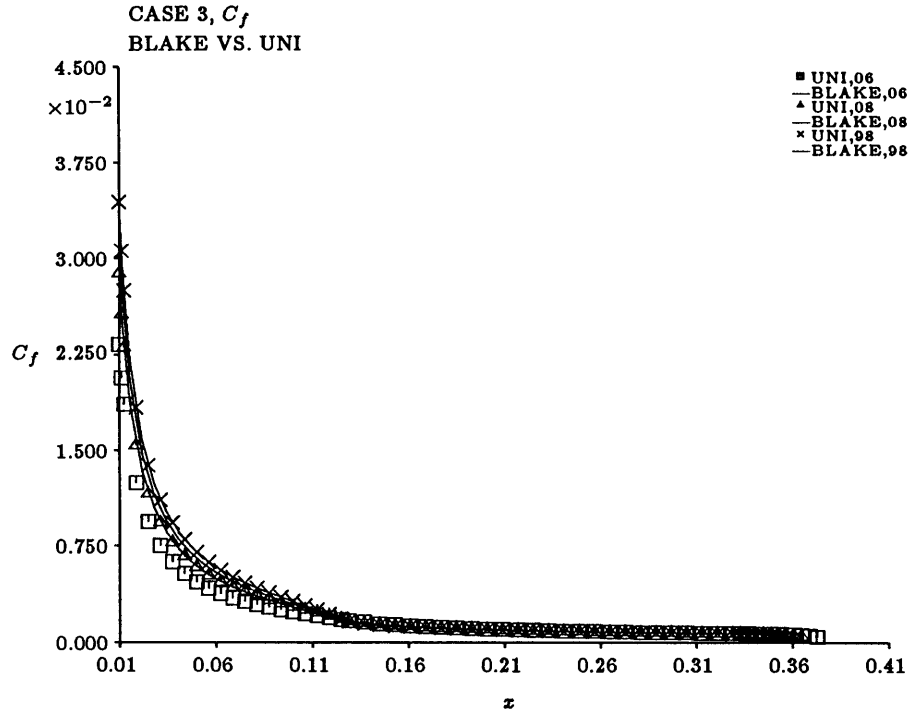

Figure 6.10: Case 3, C_f vs. x, Downstream of leading edge

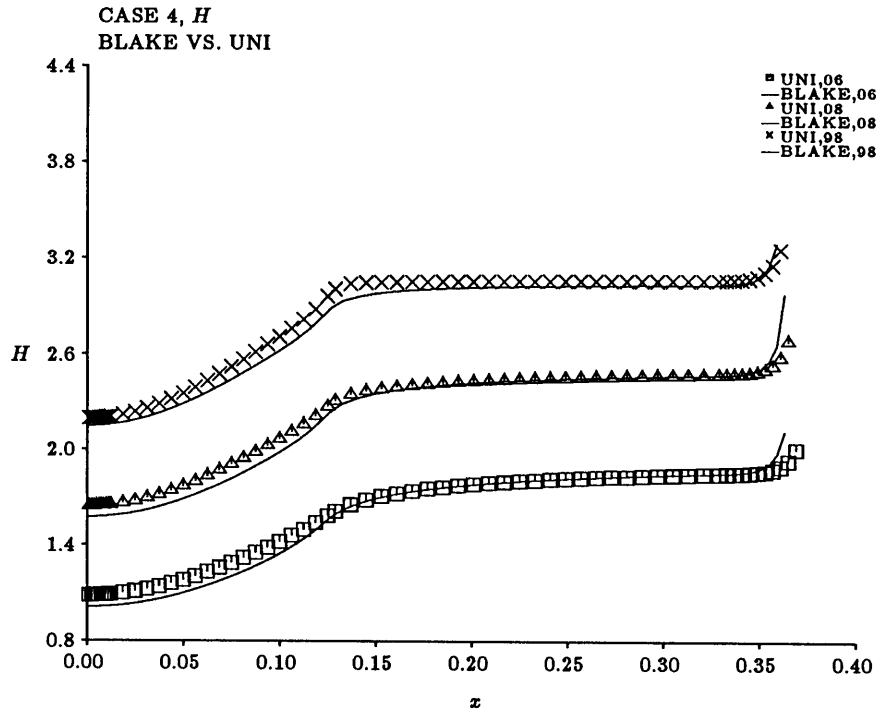

Figure 6.11: Case 4, H vs. x

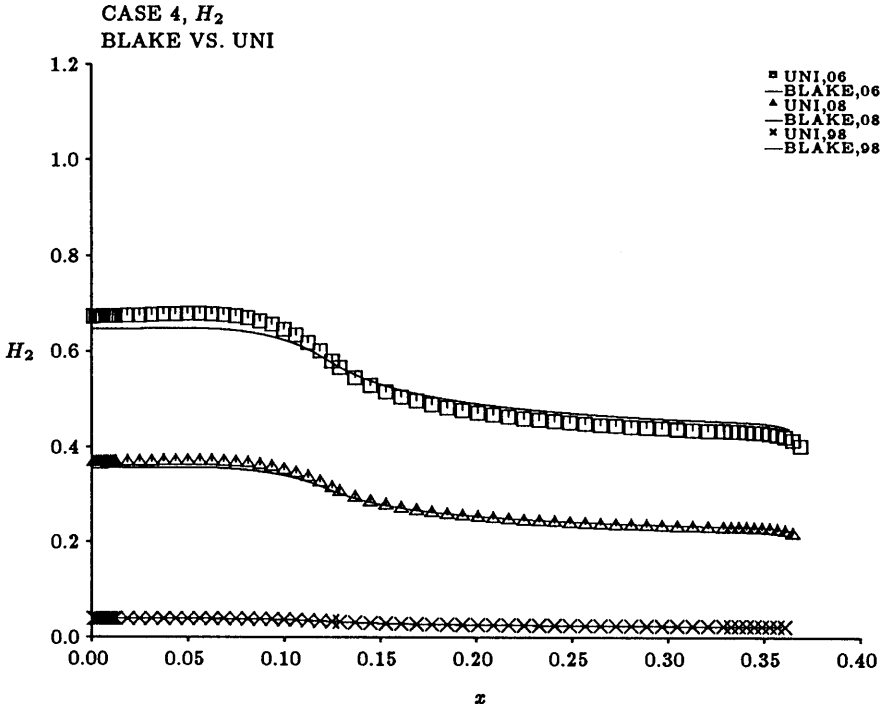

Figure 6.12: Case 4, H_2 vs. x

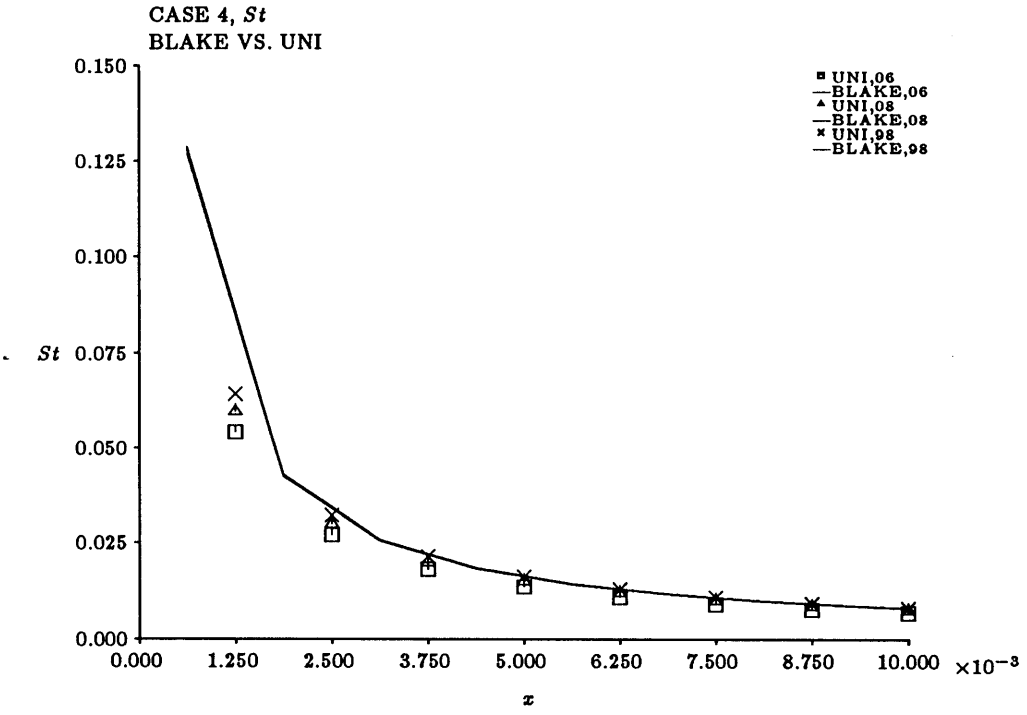

Figure 6.13: Case 4, Stanton Number vs. x, Leading Edge

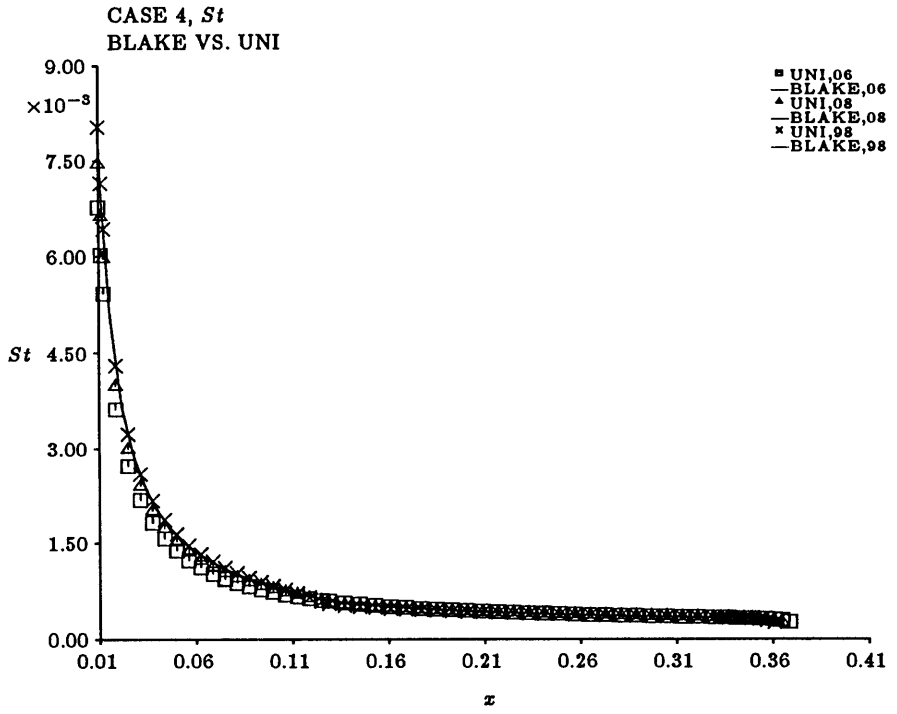

Figure 6.14: Case 4, Stanton Number vs. x, Downstream

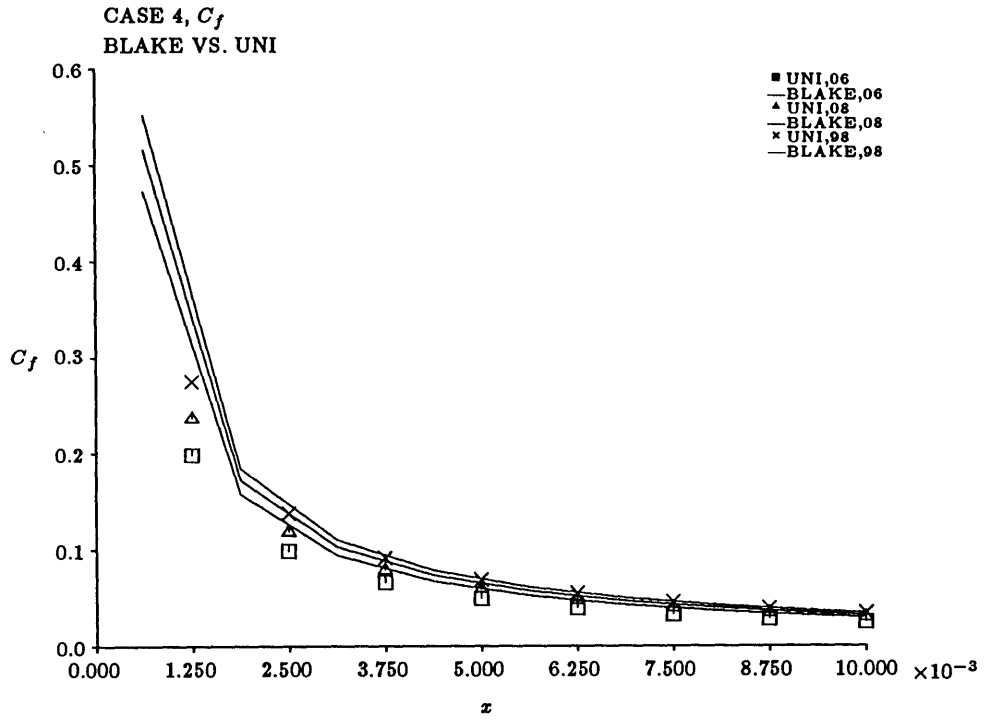

Figure 6.15: Case 4, C_f vs. x, Leading Edge

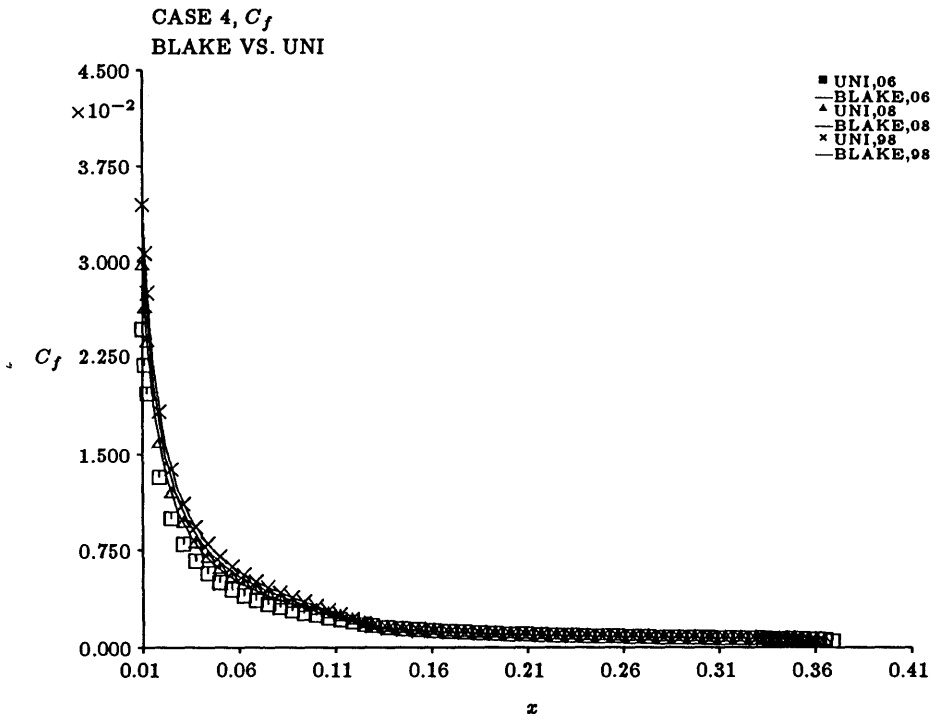

Figure 6.16: Case 4, C_f vs. x, Downstream

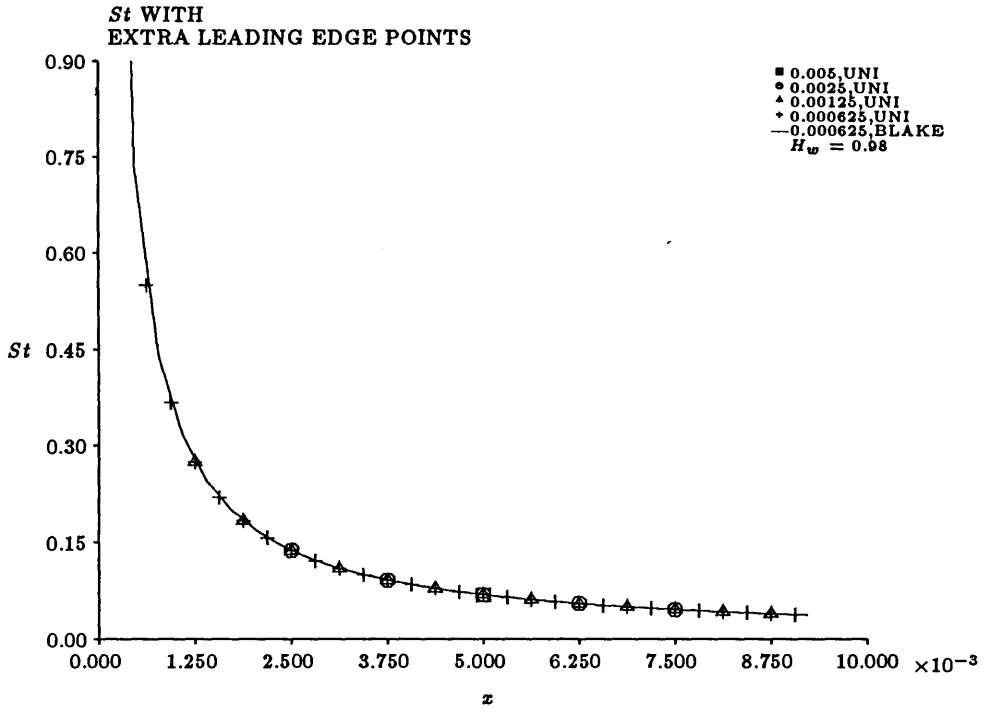

Figure 6.17: Effect of decreased space between leading edge points on the UNI solutions. The numbers indicate the streamwise position of the first analysis point. The results show that the UNI solutions are independent of the leading edge spacing. BLAKE is also independent of the leading edge spacing; a BLAKE solution is included for comparison

The leading edge difference is $< 10\%$ for all cases and quickly goes to $< 1\%$ as the solution moves downstream. At the leading edge stagnation point both St and C_f are undefined since they are normalized by the edge velocity, which is zero. The integral parameters at the leading edge are calculated by assuming similarity between the first two points. Furthermore, the first two points are assumed to be related by the Falkner-Skan wedge flow parameter β. β is calculated from the velocity distribution at the leading edge.

6.2 Comparison with experiment

UNI has been compared with two heat transfer experiments: ([17] and [7]).

6.2.1 Giedt [7]

The Giedt experiments involved airflow over circular cylinders. The Reynolds number was $Re_D = 219000$. The temperature ratio was not given. The Mach number was also not given but it is assumed to be incompressible flow and hence low Mach number. The external flow was calculated from potential flow for a cylinder in cross flow. The given Nusselt numbers were converted to Stanton numbers, normalizing with respect to the edge velocity. Figure 6.2.1 shows a comparison between UNI predictions for the heat transfer and the measured heat transfer over the cylinders. The UNI Mach number used was $M_e = 0.1$. $H_w = 0.8$ was selected, although $H_w = 0.6$, and 0.98 were similar.

Agreement between UNI and the Giedt measurements is good. The Giedt profile is the same as the first part of the simulated airfoil velocity profile used in the development test cases.

6.2.2 Nicholson [17]

The Nicholson experiments involved airflow over a set of typical commercial aircraft turbine blades. The data sets were taken at the Oxford cascade tunnel. The flow conditions were $T_0 = 430K$ and $T_w = 290K$, and $Re = 1.113 \times 10^6$. The blades are shown in Figures 6.19 and 6.21. Since UNI requires not the blade shape but the external flow, ISES [6] was used to generate the external flows for the Nicholson blades. The heat transfer data in [17] is given in terms of q_w. In order to compare the data directly with UNI output it was converted to Stanton numbers: the wall to freestream temperature difference is known, and the factor $\rho_e U_e$ can be found from the known stagnation values and the Mach number distribution given in [17], assuming that the flow is isentropic. Heat transfer predictions of UNI vs. measured

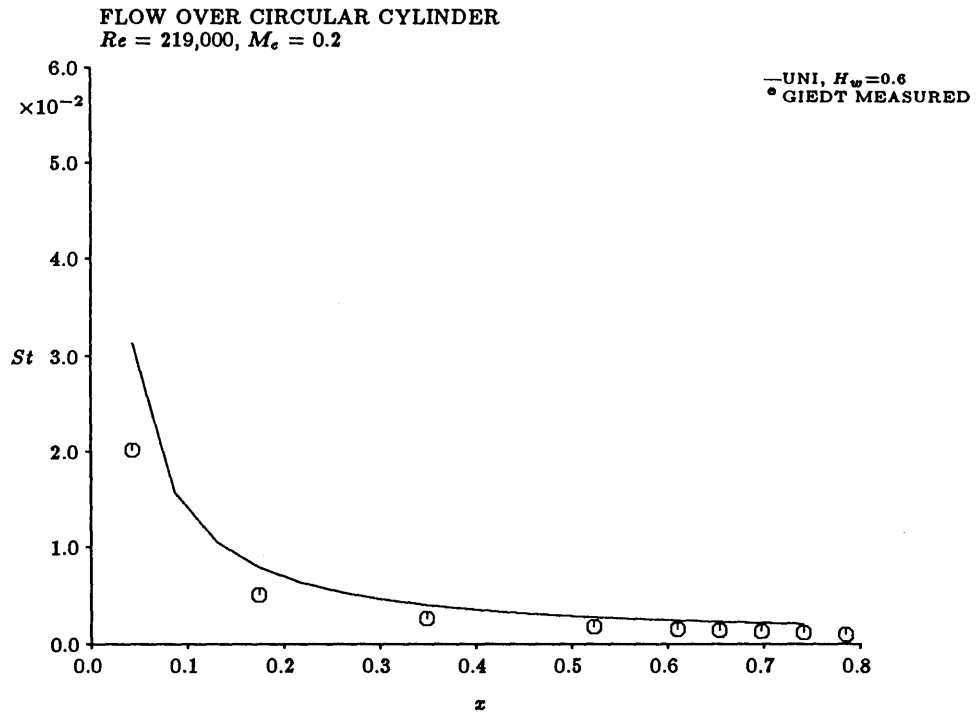

Figure 6.18: Giedt heat transfer measurements vs. UNI predictions, $\mathrm{Re}_D = 219000$, HW = 0.6, Mach number = 0.2, x is $\frac{streamwise\ distance}{diameter}$

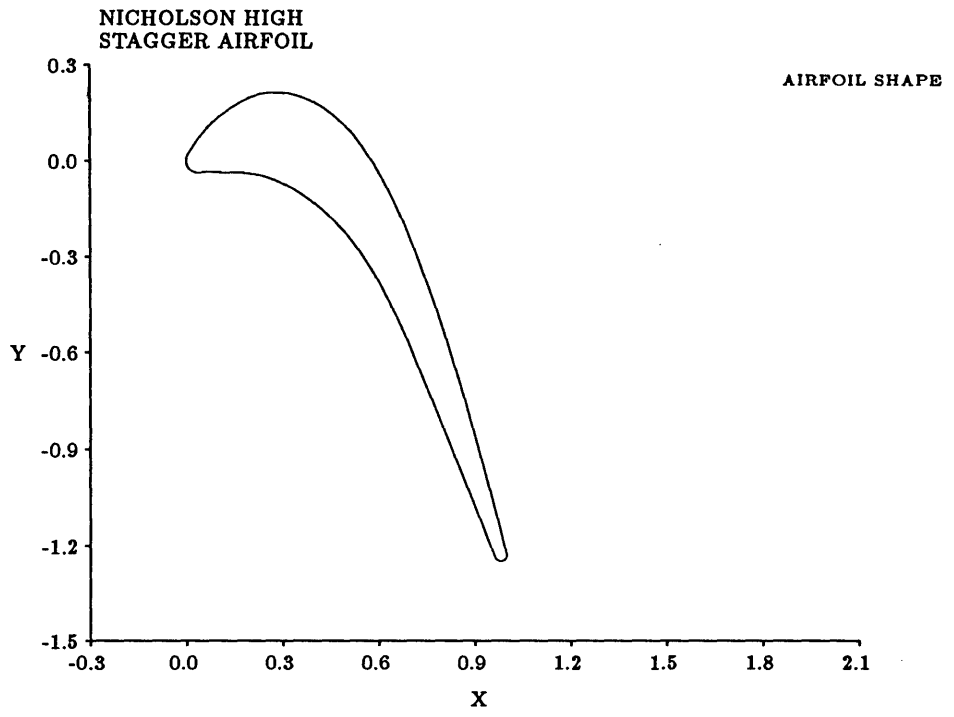

Figure 6.19: The Nicholson High Stagger Blade

quantities of [17] are shown in Figures 6.20 and 6.22. Agreement between the UNI values and those measured by Nicholson et al. is surprisingly good for the high stagger blade. The values measured are for 4% freestream turbulence. No provision is made in UNI to correct for the effects of freestream turbulence.

The Nicholson low stagger blade data was obtained from an internal Rolls Royce report [3] as well as Nicholson [17]. Like the high stagger case above the edge flow was calculated using the ISES code. The blade shape is shown in Figure 6.21. The heat transfer data from [3] was given in terms of Nusselt number. Since

$$St_x = \frac{Nu_x}{Re_x \Pr} \tag{6.1}$$

the Stanton number can be found from the other flow properties. Heat transfer predictions of UNI vs. measured quantities of the low stagger blade are shown in Figure 6.22.

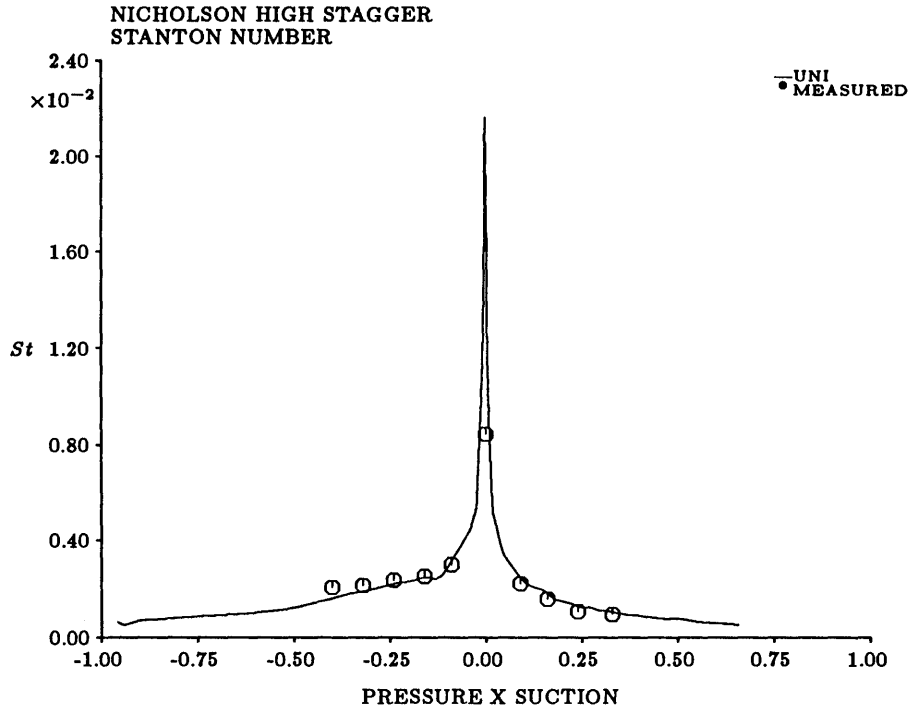

Figure 6.20: Predicted vs. measured Stanton Number for the Nicholson High Stagger Blade

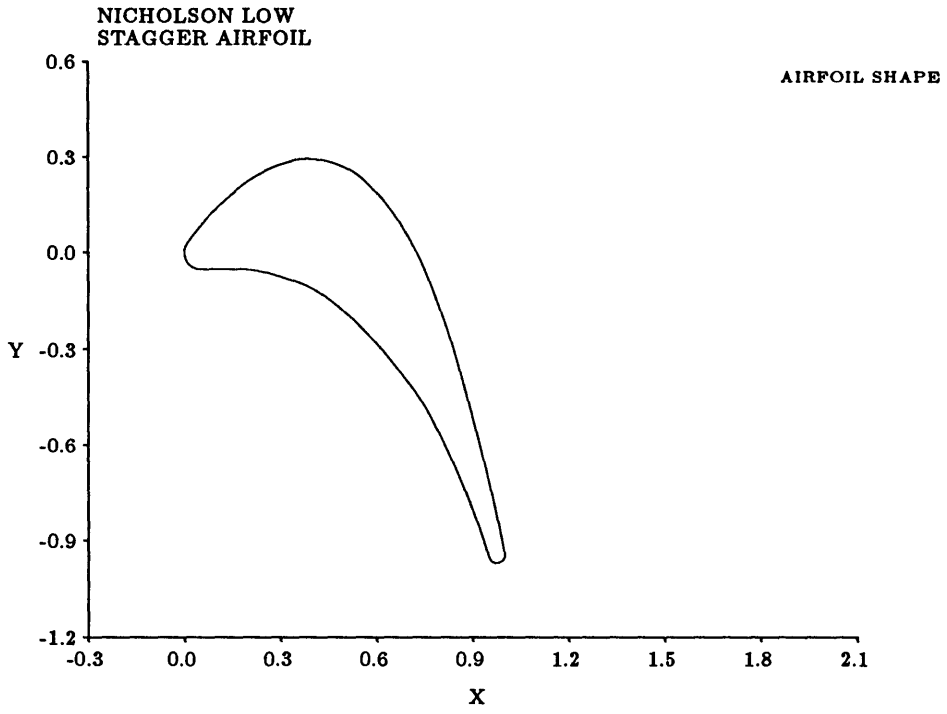

Figure 6.21: The Nicholson Low Stagger Blade

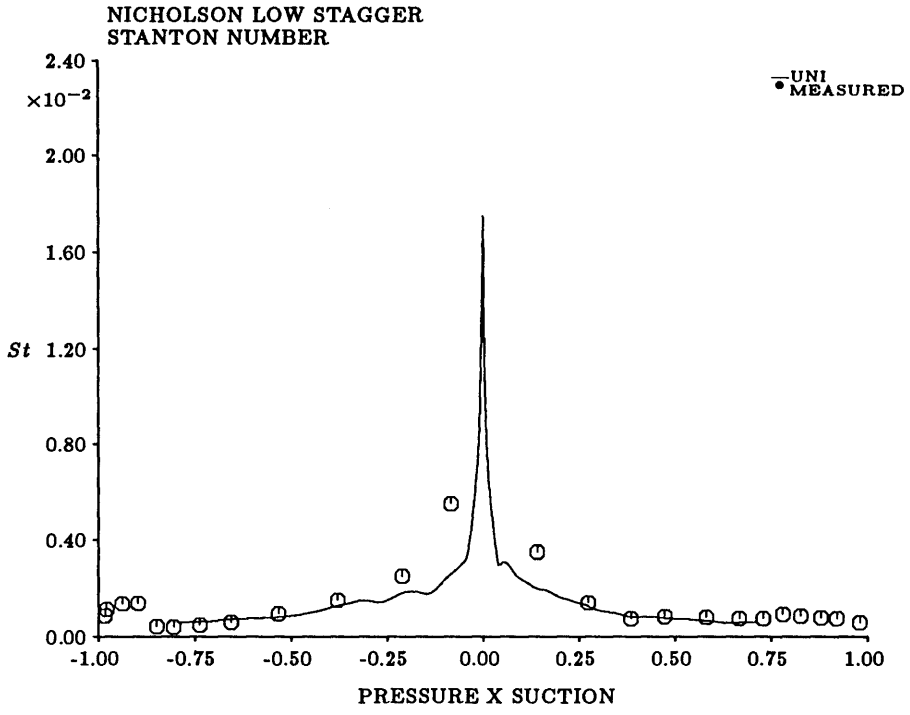

Figure 6.22: Predicted vs. measured Stanton Number for the Nicholson Low Stagger Blade

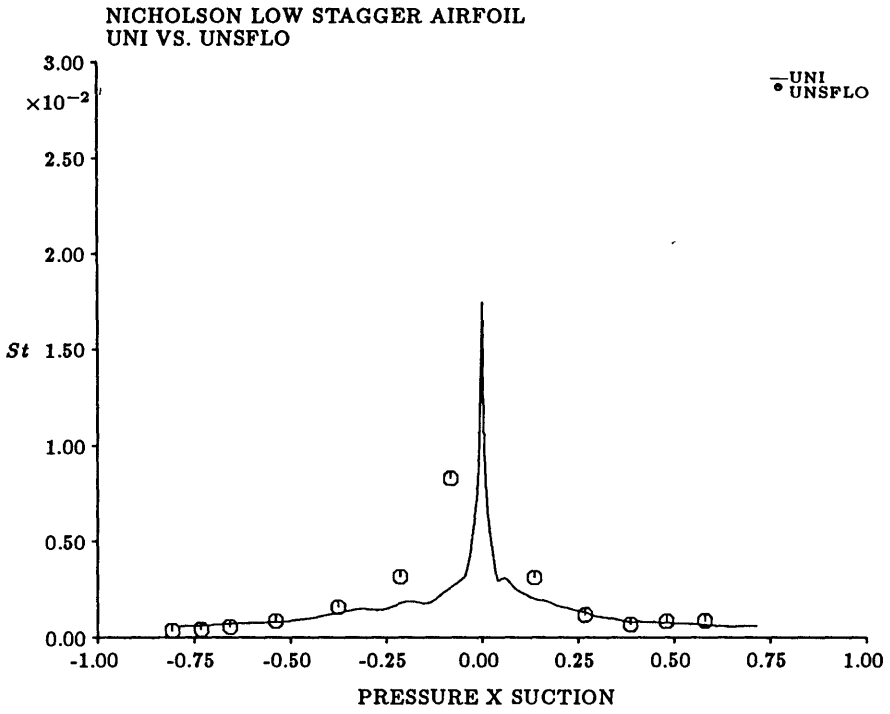

Figure 6.23: UNI Prediction vs. UNSFLO prediction for the Nicholson low stagger blade, with the stagnation point removed to show the small scale heat transfer

Agreement between UNI and the measured values of the low stagger blade are not as close as those for the high stagger blade. UNI predicts a narrow, shallow peak at $St = 0.02$; the measured values are closer to $St = 0.08$ with an exceptionally wide base.

Figure 6.23 shows the UNI predicted Stanton number vs. the Stanton number prediction of Giles' UNSFLO Navier-Stokes code [8]. UNI agrees more closely with the UNSFLO prediction than the measured data from the low stagger airfoil, especially away from the stagnation point.

Chapter 7

Discussion and Conclusions

7.1 Discussion

Green [9] states that integral heat transfer methods are not numerous. This is probably due to the difficulty in predicting the local heat transfer coefficient, and the difficulty in estimating the shape of the temperature profile across the boundary layer. In UNI, the temperature and velocity profiles are coupled together by forcing the velocity profile to conform to H_k, and forcing the total temperature profile (which is a function of both the temperature and velocity profiles) to conform to H_2. For $Pr = 1$ no other relation is needed, but for $Pr \neq 1$ some relation between δ_U and δ_T is needed. Since the forcing process is iterative, these conditions on u and T_0 can be met at each estimate of H_k and H_2, then checked against the residuals of the three basic equations (Eqs. 5.1, 5.2, and 5.3).

The results of the development tests show that UNI agrees well with the finite difference code BLAKE. This is not all that unexpected since two important factors: the integral wall heat transfer scheme, and the C_D correction for non-uniform viscosity were obtained from BLAKE results. Since UNI is to be part of a design code, it is important that it accurately predict trends in heat transfer and aerodynamic efficiency. In this way, different designs can be compared as to their aerodynamic and heat transfer preformance. UNI has shown that it accurately predicts heat transfer and aerodynamic loss performance trends. It is also important that it give good absolute local heat transfer and aerodynamic loss predictions. UNI's developmental cases show that it can predict local values to better than 10% accuracy as compared with finite difference codes. However, since UNI is an integral method, it is well suited to be integrated into the ISES airfoil design and analysis code.

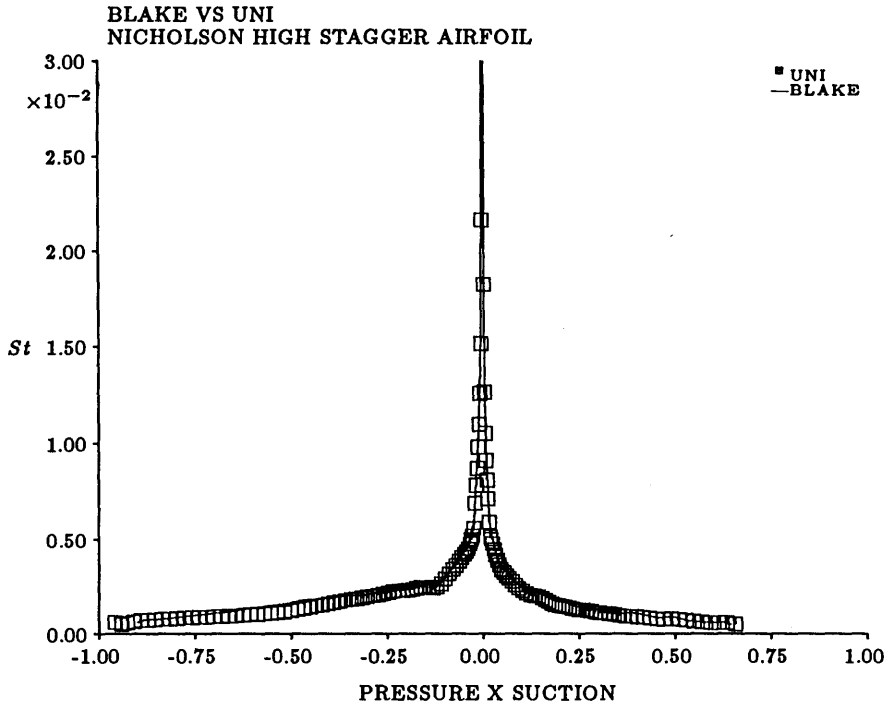

Figure 7.1: Comparison of BLAKE and UNI Predictions for the Nicholson High Stagger Blade

Agreement with experiment is not as good as with theory. This seems to be a common problem in turbine analysis, but that does not excuse further efforts. Agreement with Giedt and the Nicholson high stagger case is good; agreement with the low stagger data is not as good. Prediction of St and C_f at the leading edge are not good, but if the subsequent analysis points are closely spaced near the leading edge, greater accuracy is possible. A comparison between BLAKE and UNI for the Nicholson flows shows that the two codes agree quite closely (Figures. 7.1 and 7.2).

For a typical development case (Flow 6, $H_w = 0.6$) UNI is ~40% faster than BLAKE yet gives comparible results for the integral parameters, heat transfer, skin friction, all of course for the laminar case. For ISES and UNSFLO, accuracy is highly dependent on the number of grid points, and so is the time needed to converge. For the viscous portion of the Nicholson low

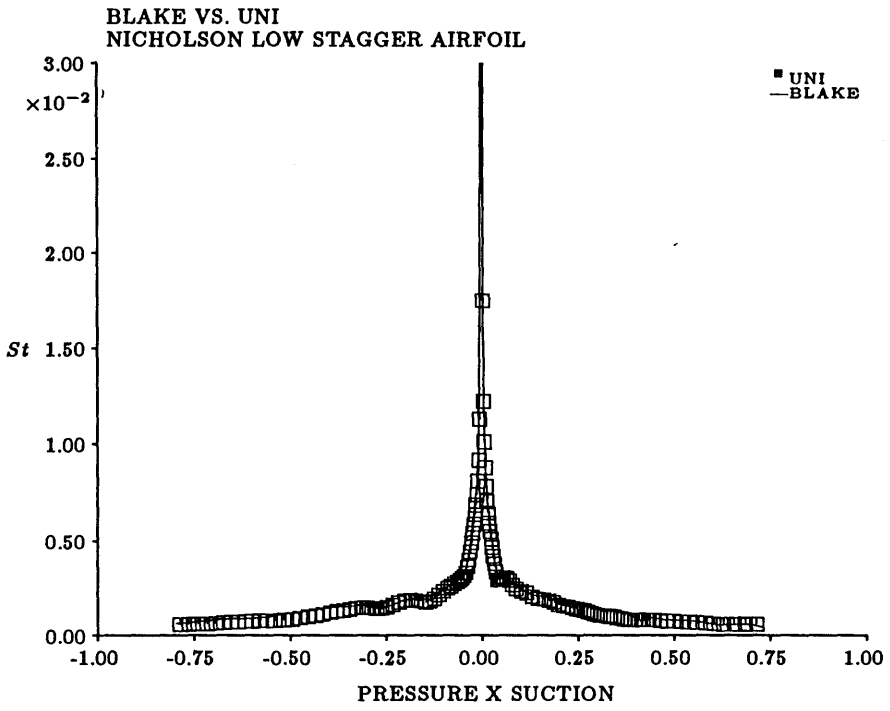

Figure 7.2: Comparison of BLAKE and UNI Predictions for the Nicholson Low Stagger Blade

stagger case ISES converged to the same rms remainder ~15 times faster than did UNSFLO for the same number of grid points. This is not to say that their accuracies are identical. When the non-adiabatic boundary layer scheme is incorporated into ISES, convergence will probably be slower since H_k is no longer an algebraic relationship with M_e^2 and H. H_k is now found iteratively through H, M_e^2, H_2, and the perturbation coefficient, P.

The most obvious shortcoming of this program is its inability to deal with turbulent flow. In [5] Drela states that for turbulent flow, the primary scaling factor for the wall layer is the skin friction. In Chapter 3 of [9] Green discussed a method for determining the skin friction with non-adiabatic flow. It is suggested that this method, in conjuction with the enthalpy thickness analysis also suggested by Green and developed here would be a good starting point for an integral non-adiabatic turbulent flow analysis. Because of the difficulty of correlating the temperature effects with the dissipation and skin friction the extension of this method to

turbulent flow will probably be difficult. The shape of the turbulent boundary layer would not be well represented by a third order polynomial. Some way of modelling the layers of turbulent temperature and velocity boundary layers would have to be devised in order to accurately predict H_k. For turbine applications the turbulent extension of this code would definitely be necessary for any practical use.

This code probably could be refined to give greater accuracy at all points in the flow with better correlations. As was noted for the dissipation coefficient, a correlation to the wall temperature was needed to account for temperature and hence viscosity gradients in the boundary layer. This correlation, the integral heat transfer prediction correlation, and most importantly the H_k estimation scheme could be improved to better account for interaction between such factors as the Prandtl number, the freestream pressure gradient, and the wall temperature. A correction for freestream turbulence could also be used.

7.2 Conclusions

Although traditionally turbine airfoil design has tried to optimize aerodynamic efficiency, the potential exists to increase total cycle efficiency by considering heat transfer performance at the design stage. The ISES airfoil design and analysis tool is an adiabatic code that has the potential to design turbine airfoils if modified to allow non-adiabatic boundary conditions. With such a tool turbine airfoils could be designed to tradeoff aerodynamic efficiency and heat transfer performance to reach the highest level of total cycle efficiency.

Radiation heat transfer was found to have a minor role in heat transfer to a turbine blade compared to convection heat transfer. Since the percentage of heat transferred by radiation is ¡10%, reductions in radiative heat transfer do not have as much potential for reducing the total heat transfer as do reductions in the convectional heat transfer.

Using a diffusion factor model it was shown that a point of minimum aerodynamic losses

exists, and that by sacrificing some amount of aerodynamic efficiency lower heat transfer can be achieved. In a total cycle analysis the point of highest total efficiency might not be at the point of highest aerodynamic efficiency, and if so designing for low heat load would increase the total cycle efficiency.

The non-adiabatic integral boundary layer model was chosen over finite difference codes in view of the number of variables to be solved. Since the computational time and effort required is strongly dependent on the number of points involved, an integral method has an advantage. And, as shown in Chapter 6, the accuracy of the two methods is comparable.

A new integral correlation for heat transfer has been developed from the finite difference code BLAKE [4] solutions to the developmental test case flows. It is surprisingly simple and highly accurate for Reynolds numbers between $1. \times 10^5$ and $1. \times 10^7$, Prandtl numbers between 0.7 and 1.0, and pressure gradients measured by the Falkner-Skan parameter between $\beta = 0$ and $\beta = 1$. Since these flow conditions are typical of turbine blade leading edge values this method should be useful for leading edge heat transfer prediction.

Bibliography

[1] Ainley, A.M., and Mathieson, G.C.R. "A Method of Performance Estimation for Axial-Flow Turbines," A.R.C.R.&M. No. 2974, 1957.

[2] Anderson, D.A., Tannehill, J.C., and Pletcher, R.H. Computational Fluid Mechanics and Heat Transfer, Hemisphere Publishing Company, Washington, D.C. 1984.

[3] Connell, S.D. "An Evaluation of FANSI-2D Version 2.10." Theoretical Science Group Report TSG0222, Rolls-Royce Limited.

[4] Drela, M. "A New Transformation and Integration Scheme for the Compressible Boundary Layer Equations, and Solution Behavior at Separation," MIT Gas Turbine and Plasma Dynamics Laboratory Report No. 172, May 1983.

[5] Drela, M. "Two-Dimensional Transonic Aerodynamic Design and Analysis Using the Euler Equations," MIT Gas Turbine Laboratory Report No. 187, February 1987.

[6] Drela, M., and Giles, M.B. "ISES: A Two-Dimensional Viscous Aerodynamic Design and Analysis Code," AIAA-87-0424, 1987.

[7] Giedt, W.H. "Investigation of Variation of Point Unit Heat-Transfer Coefficient Around a Cylinder Normal to an Air Stream." Transactions of the ASME. Vol. 71, pgs. 375-381, 1949.

[8] Giles, Michael. "UNSFLO: A Numerical Method for Unsteady Inviscid Flow in Turbomachinery." Gas Turbine Lab Report No. 195, October, 1988.

[9] Green, J.E. "Application of Head's Entrainment Method to the Prediction of Turbulent Boundary Layers and Wakes in Compressible Flow," A.R.C.R.&M. No. 3788, 1976.

[10] Guenette, G.R., Epstein, A.H., Giles, M.B., and Haimes, R. "Fully Scaled Transonic Turbine Rotor Heat Transfer Measurements," Prepublication Draft, 1987.

[11] Holman, J.P. Heat Transfer, Sixth Edition. McGraw-Hill Book Company, New York, 1986.

[12] Horlock, J.H. Axial Flow Turbines, Butterworth and Company, 1966.

[13] Johnsen, I.A., and Bullock, R.O. "Aerodynamic Design of Axial-Flow Compressors," NASA SP-36, NASA Scientific and Technical Information Division, 1965.

[14] Kerrebrock, J.L. Aircraft Engines and Gas Turbines, MIT Press, 1987.

[15] McAdams, W.H. Heat Transmission, Chapter 4, "Radient Heat Transmission," by Hoyt C. Hottel. McGraw-Hill Book Company, 1954.

[16] Moustapha, S.H., Okapuu, U., and Williamson, R.G. "Influence of Rotor Blade Aerodynamic Loading on the Performance of a Highly Loaded Turbine Stage", ASME 86-GT-56, 1986.

[17] Nicholson, J.H., Forest, A.E., Oldfield, M.L.G., and Schultz, D.L. "Heat Transfer Optimised Turbine Rotor Blades – An Experimental Study Using Transient Techniques," ASME 82-GT-304, 1982.

[18] Schlichting, Hermann. Boundary Layer Theory, McGraw-Hill Book Co. Inc., London, 1955.

[19] Schmidt, Ernst, and Wenner, Karl. "Heat Transfer Over the Circumference of a Heated Cylinder in Transverse Flow." NACA TM-1050, 1943.

[20] Schwab, J.R., Stabe, R.G. and Whitney, W.J. "Analytical and Experimental Study of Flow Through an Axial Turbine Stage With a Nonuniform Inlet Radial Temperature Profile," NASA Technical Memorandum 83431, AIAA-83-1175, 1983.

[21] Smith S.F. "A Simple Correlation of Turbine Efficiency," Journal of the Royal Aeronautical Society, Vol. 69, July 1965.

[22] Stewart, W.L., Whitney, W.J., and Wong, R.Y. "A Study of Boundary-Layer Characteristics of Turbomachinery Blade Rows and Their Relation to Over-All Blade Loss," Transactions of the ASME, Journal of Basic Engineering, September 1960.

[23] Van Wylan, G.J., Sonntag, R.E. Introduction to Thermodynamics Classical and Statistical Second Edition, John Wiley and Sons, New York, 1982

[24] White, F.M. Viscous Fluid Flow, McGraw-Hill, 1974.

Appendix A

Gasseous Radiant Heat Transfer

The mean beam length analysis for gasseous radiant heat transfer is one way of looking at a complex problem. It is semi-empirical in that it applies empirical corrections to the theoretical gas heat transfer equation (Eq. 3.4). The empiricism comes in through the calculation of ϵ_G and α_G of the gas.

The mean beam length is a non-physical length that takes into account the geometry of the situation. A general rule of thumb for its calculation is $L_{MB} = 3.6\frac{VOLUME}{AREA}$. For several specific geometries less general formulae are given in [11]. For the turbine application the geometry was modeled as the radiation of a volume of gas in a cylinder to the surface. The diameter was modeled as the blade pitch, for this case ~ 1.3 inches. Holman suggests $L_{MB} = 0.95D$, and in this case $L_{MB} = 0.105$ feet was used.

Calculations were made at 500°F intervals (3000°–5000°F) and at 10 atmosphere pressure intervals (10–40 atm.) The combustion chemistry was modeled as follows. Assume a hydrocarbon fuel (methane) and the following reaction:

$$CH_4 + 2O_2 \rightarrow 2H_2O + CO_2 \tag{A.1}$$

If we have a 0.03 fuel to air mass ratio [14] the chemsitry would look something like this. Since air is approximately $3O_2 + 7N_2$ the actual reaction would be:

$$6O_2 + 14N_2 + CH_4 \rightarrow 2H_2O + CO_2 + 14N_2 + 4O_2 \tag{A.2}$$

It is assumed that the oxygen and nitrogen do not radiate since their emittances are small compared to carbon dioxide and water vapor [11]. The partial pressures for both CO_2 and H_2O are needed; an intermediate step is to calculate the product $p_{CO_2}L_{MB}$ and $p_{H_2O}L_{MB}$.

These are compared to Figures 8-34 and 8-35 in [11] to find the emissivity ϵ_{CO_2} and ϵ_{H_2O}. Correction factors C_{CO_2} and C_{H_2O} are applied to correct for the given total pressure, and a final correction $\Delta\epsilon$ is calculated since both CO_2 and H_2O are present. The final formula for ϵ is:

$$\epsilon_G = C_{CO_2}\epsilon_{CO_2} + C_{H_2O}\epsilon_{H_2O} - \Delta\epsilon \tag{A.3}$$

α_G is calculated in a similar fashion [11, pgs. 419-420].

The convectional heat transfer is calculated by assuming a representative Nusselt number from [10]. The same temperatures were used as above, but no correction for the different pressure ratios was attempted.

Despite the T^4 behavior of radiational heat transfer this analysis does not show the expected sharp increase in the ratio of radiational heat transfer to total heat transfer as the TET increases to the stoichiometric limit. This analysis should not be taken as the final word on the subject since several values in the analysis were approximate at best. No allowance was made for particulates in the flow, nor the role that chemistry would undoubtedly have in such high temperature flows. Still, not even a strong trend toward a great role for radiational heat transfer was found.

Appendix B

Derivation of Fundamental equations

We start from three basic equations:

Continuity:

$$\frac{\partial}{\partial x}(\rho u) + \frac{\partial}{\partial x}(\rho v) = 0 \tag{B.1}$$

Streamwise Momentum:

$$\rho u \frac{\partial u}{\partial x} + \rho v \frac{\partial v}{\partial y} = \rho_e U_e \frac{dU_e}{dx} + \frac{\partial \tau}{\partial y} \tag{B.2}$$

and from [9, Appendix A] the enthalpy equation:

$$\frac{d}{dx}(\rho_e U_e \theta H_2) = \frac{q_w}{C_p T_{0e}} \tag{B.3}$$

where x is the streamwise coordinate and y is the normal coordinate.

Summing u(B.1) + (B.2) and integrating over the boundary layer we have

$$\int_0^{y_e} (u\frac{\partial}{\partial x}\rho u + u\frac{\partial}{\partial y}\rho v + \rho u\frac{\partial u}{\partial x} + \rho v\frac{\partial v}{\partial y})dy = \int_0^{y_e} (\rho_e U_e \frac{dU_e}{dx} + \frac{\partial \tau}{\partial y})dy \tag{B.4}$$

Noting that:

$$\frac{\partial}{\partial x}(\rho u^2) = \frac{\partial \rho}{\partial x}u^2 + 2\rho u\frac{\partial u}{\partial x} \tag{B.5}$$

$$\frac{\partial}{\partial y}(\rho u v) = u\frac{\partial}{\partial y}(\rho v) + \rho v\frac{\partial u}{\partial y} \tag{B.6}$$

$$\int_0^{y_e} \frac{\partial}{\partial y}(\rho u v)dy = \rho_e U_e v_e \tag{B.7}$$

and from continuity:

$$\rho_e v_e = \int_0^{y_e} \frac{\partial}{\partial y}(\rho v)dy = -\int_0^{y_e} \frac{\partial}{\partial x}(\rho u)dy \tag{B.8}$$

and from the definition of τ_w:

$$\int_0^{y_e} \frac{\partial \tau}{\partial y} dy = -\tau_w \tag{B.9}$$

we have:

$$\int_0^{y_e} (\frac{\partial}{\partial x}(\rho u^2) - \rho_e U_e \frac{dU_e}{dx} - U_e \frac{\partial}{\partial x}(\rho u)) dy = -\tau_w \tag{B.10}$$

Note that

$$\frac{\partial}{\partial x}(\rho u(U_e - u)) = U_e \frac{\partial}{\partial x}(\rho u) - \frac{\partial}{\partial x}(\rho u^2) + \rho_e U_e \frac{dU_e}{dx} \tag{B.11}$$

Combining terms and introducing C_f

$$\frac{\partial}{\partial x} \int_0^{y_e} (\rho u(U_e - u)) dy + \frac{dU_e}{dx} \int_0^{y_e} (\rho_e U_e - \rho u) dy = \frac{C_f}{2} \rho_e U_e^2 \tag{B.12}$$

Divide by $\rho_e U_e^2$ and introduce the definitions of θ and δ^* yields

$$\frac{1}{\rho_e U_e^2} \frac{\partial}{\partial x}(\rho_e U_e^2 \theta) + \frac{1}{U_e} \frac{dU_e}{dx} \delta^* = \frac{C_f}{2} \tag{B.13}$$

expanding and rewriting yields

$$\frac{\partial \theta}{\partial x} + \frac{2\theta}{U_e} \frac{dU_e}{dx} + \frac{\theta}{\rho_e} \frac{\partial \rho_e}{\partial x} + \frac{1}{U_e} \frac{dU_e}{dx} \delta^* = \frac{C_f}{2} \tag{B.14}$$

From thermodynamic relations [23] we know

$$\frac{1}{\rho_e} \frac{\partial \rho_e}{\partial x} = -\frac{M_e^2}{U_e} \frac{dU_e}{dx} \tag{B.15}$$

and introducing the definition of H we have

$$\frac{\partial \theta}{\partial x} + \frac{\theta}{U_e} \frac{dU_e}{dx} (2 + H - M_e^2) = \frac{C_f}{2} \tag{B.16}$$

which is the first of the three integrated equations. To get the second of the three integrated equations we start from $(u^2 - U_e^2)$(B.1)+$2u$(B.2)

This can be grouped as

$$(u^2\frac{\partial}{\partial x}(\rho u) + 2\rho u^2\frac{\partial u}{\partial x} - U_e^2\frac{\partial}{\partial x}(\rho u) - 2\rho_e U_e u\frac{dU_e}{dx}) + ((u^2 - U_e^2)\frac{\partial}{\partial y}(\rho v) + 2\rho uv\frac{\partial v}{\partial y}) - 2u\frac{\partial \tau}{\partial y} = 0 \tag{B.17}$$

Note that

$$\frac{\partial}{\partial x}(\rho u(u^2 - u_e^2)) + 2uU_e\frac{dU_e}{dx}(\rho - \rho_e) = u^2\frac{\partial}{\partial x}(\rho u) + 2\rho u^2\frac{\partial u}{\partial x} - U_e^2\frac{\partial}{\partial x}(\rho u) - 2\rho_e U_e u\frac{dU_e}{dx} \tag{B.18}$$

also

$$\frac{\partial}{\partial y}(\rho v(u^2 - U_e^2)) = (u^2 - U_e^2)\frac{\partial}{\partial y}(\rho v) + 2\rho uv\frac{\partial u}{\partial y} \tag{B.19}$$

Substituting into eq. (B.17) yields

$$\frac{\partial}{\partial x}(\rho u(u^2 - U_e^2)) + 2uU_e\frac{dU_e}{dx}(\rho - \rho_e) + \frac{\partial}{\partial y}((u^2 - U_e^2)\rho v) = 2u\frac{\partial \tau}{\partial y} \tag{B.20}$$

Regrouping to form the integrands of θ^* and δ^{**} and integrating over the boundary layer yields

$$\frac{\partial}{\partial x}(-\rho_e U_e^3\theta^*) - 2\rho_e U_e^2\frac{dU_e}{dx}\delta^{**} + ((u^2 - U_e^2)\rho v)\mid_0^{y_e} = 2(u\tau\mid_0^{y_e} - \int_0^{y_e}(\tau\frac{\partial u}{\partial y})dy) \tag{B.21}$$

The evaluated quantities go to zero since they are zero at the wall and at the boundary layer edge. Noting this and bringing in the definition of C_D yields

$$\frac{\partial}{\partial x}(\rho_e U_e^3\theta^*) + 2\rho_e U_e^2\frac{dU_e}{dx}\delta^{**} = 2\rho_e U_e^3 C_D \tag{B.22}$$

Dividing by $\rho_e U_e^3$, expanding the derivative and introducing eqn. (B.15) yields

$$(3 - M_e^2)\frac{\theta^*}{U_e}\frac{dU_e}{dx} + \frac{\partial \theta^*}{\partial x} + 2\frac{\delta^{**}}{U_e}\frac{dU_e}{dx} = 2C_D \tag{B.23}$$

Take eqn. (B.16), multiply by H^*, add $\frac{\theta^*}{U_e}\frac{dU_e}{dx}$ to both sides and regroup to yield

$$(3 - M_e^2)\frac{\theta^*}{U_e}\frac{dU_e}{dx} = H^*(\frac{C_f}{2} - \frac{d\theta}{dx}) - (H - 1)\frac{\theta^*}{U_e}\frac{dU_e}{dx} \tag{B.24}$$

Substitute into eqn. (B.23). Note that

$$\theta\frac{dH^*}{dx} = \frac{\partial \theta^*}{\partial x} - H^*\frac{\partial \theta}{\partial x} \tag{B.25}$$

Regroup and rewrite to form

$$\theta\frac{dH^*}{dx} + (2H^{**} - H^*(H - 1))\frac{\theta}{U_e}\frac{dU_e}{dx} = 2C_D - H^*\frac{C_f}{2} \tag{B.26}$$

which is the second of the three equations. To get the third equation we start with the enthalpy equation, expand the derivative and assume that the recovery factor is constant in x [24]. This yields

$$\theta\frac{dH_2}{dx} + H_2\frac{d\theta}{dx} + \frac{\theta H_2}{\rho_e}\frac{d\rho_e}{dx} + \frac{\theta H_2}{U_e}\frac{dU_e}{dx} = \frac{q_w}{\rho_e U_e C_p T_{0e}} \tag{B.27}$$

Introducing eqs. (B.15) and (B.16) and regrouping yields

$$\theta\frac{dH_2}{dx} = Q - H_2(\frac{C_f}{2} - (H + 1)\frac{\theta}{U_e}\frac{dU_e}{dx}) \tag{B.28}$$

which is the third equation.